SYNTHESIS AND SINTERING 5 (2025) 259–283

Available online at www.synsint.com

Synthesis and Sintering

ISSN 2564-0186 (Print), **ISSN** 2564-0194 (Online)

Review article

A high-impact review on M-type hexaferrites: Structural, magnetic and microwave absorption characteristics with emerging trends

Seyed Salman Seyed Afghahi [a,*], **Reza Torkamani** [b], **Pouria Dehghani** [a]

[a] *Department of Engineering, Imam Hossein University, Tehran, Iran*
[b] *Faculty of Physics, University of Tabriz, Tabriz, Iran*

A B S T R A C T

The use of absorbers is critical for protecting human health, enabling stealth applications, and preventing electromagnetic interference. Although various absorbers have been developed in recent years, many suffer from poor synergy and low attenuation efficiency, resulting in limited performance. Also, the factors affecting the increase in the effective absorption bandwidth have not been well addressed. Hexaferrites, with their ability to provide magnetic loss along with dielectric loss, are promising candidates for microwave absorbers. However, hexaferrites currently lack the necessary efficiency, and their microwave attenuation properties need to be enhanced. In this review article, we examine recent studies on M-type hexaferrites, focusing on the parameters influencing microwave absorption properties. The magnetic properties of these materials, along with the origins of their magnetic behavior, the structural characteristics, and various synthesis methods of hexaferrites, are thoroughly analyzed due to their significant impact on absorption performance. Finally, in this review article, we present suggestions that can lead to improved efficiency and use of hexaferrites in industry as adsorbents.

KEYWORDS

M-type hexaferrites
Structural properties
Magnetic properties
Microwave absorption properties

OPEN ACCESS

Nomenclature

Symbol	Definition	Symbol	Definition	Symbol	Definition
M_s	Saturation magnetization	m_B	Magnetic moment per unit	E_{MC}	Energy of crystalline magnetic anisotropy
H_a	Anisotropy	M_r	Remanent magnetization	N_d	Demagnetization factor
T_c	Curie temperature	K_1	Crystalline magnetic anisotropy constant	W_p	Domain wall energy density
BaM	$BaFe_{12}O_{19}$	H_{Ci}	Intrinsic coercivity	K_b (erg/K)	Boltzmann constant
SrM	$SrFe_{12}O_{19}$	μ_0	Vacuum permeability	VSM	Vibrating sample magnetometer
PbM	$PbFe_{12}O_{19}$	SQR	Squareness ratio	H_d	Demagnetizing field
XRD	X-ray diffraction	E_{shape}	Energy of shape anisotropy	RL	Reflection loss
SEM	Scanning electron microscopy	$E_{surface}$	Energy of surface anisotropy	Z_{in}	Input impedance
H_c	Coercivity field	E_{ME}	Energy of stress-induced anisotropy	Z_0	Air impedance

* Corresponding author. *E-mail address:* afghahi@ihu.ac.ir (S.S. Seyed Afghahi)
Received 17 August 2025; Received in revised form 30 September 2025; Accepted 11 October 2025.

https://doi.org/10.53063/synsint.2025.54306

Nomenclature

Symbol	Definition	Symbol	Definition	Symbol	Definition
ε_r	Relative permeability	tan δ_m	Magnetic loss	H_{eff}	Effective magnetic field
ε'	Real part of relative permeability	α	Attenuation constant	H_{int}	Interaction field
ε''	Imaginary part of relative permeability	d_m	Impedance matching	H_r	Resonance field
μ_r	Relative permittivity	f_m	Matching frequency	ΔH	Ferromagnetic resonance linewidth
μ'	Real part of relative permittivity	ε_s	Static dielectric constant	ΔH_a	Crystalline anisotropy linewidth
μ''	Imaginary part of relative permittivity	ε_∞	High-frequency relative dielectric constant	ΔH_p	Intrinsic linewidth
tan δ_e	Dielectric loss	f_r	Resonance frequency	ΔH_i	Porosity linewidth

1. Introduction

Due to advancements in technology, the use of electromagnetic waves, particularly microwaves, has increased significantly [1–3]. However, the negative effects associated with their use have also grown in proportion. Researchers have categorized microwave spectra into various bands for application in different fields [4]. These bands are shown in Fig. 1a. Microwaves are commonly used in most wireless communications, radar systems, satellites, and devices such as Wi-Fi, smartphones, and smart cars (Fig. 1b) [5]. The increased usage of these waves has led to some issues. Certain devices experience interference when exposed to microwave radiation [6–10]. Additionally, prolonged human exposure to electromagnetic waves can result in various diseases and even cancer [11, 12]. In the military sector, the use of absorbers that can generate a large absorption bandwidth and high attenuation is crucial for stealth applications [13–16]. Therefore, it is necessary to develop absorbers that can address these issues effectively.

A variety of materials for microwave absorption have been introduced in recent years. The microwave absorption properties of materials such as activated carbon [17–19], carbon nanotubes [8, 20–22], metal oxides [23–25], MXenes [26–28], metal-organic frameworks (MOFs) [29, 30], and ferrites [31–35] have been extensively studied by researchers. Additionally, the absorption mechanisms in these materials have been partially explained. However, it remains essential to clearly identify the factors that improve absorber efficiency. Ferrites, especially hexaferrites, have garnered a lot of interest in a variety of sectors because of their high M_s [36–38], cost-effective production [39–41], large H_a [42, 43], high electrical resistivity [44, 45], favorable magnetoelectric properties [46–48], high T_C [49–51] and excellent chemical stability [52–54]. Despite these advantages, these materials exhibit low absorption efficiency and high density. Therefore, by improved design and the addition of different chemicals, it is required to improve the microwave absorption capabilities of hexaferrites.

One of the key applications of hexaferrites lies in microwave absorption. More research has been done on the microwave absorption characteristics of M-type hexaferrites than on any other hexaferrite. Hexaferrites possess a complex crystal structure, which makes it challenging to analyze the mechanisms of microwave energy loss within them. On the other hand, when hexaferrites are combined with other materials, they can synergistically enhance both the dielectric and magnetic components, thereby increasing energy loss. Thus, a comprehensive review of research conducted on M-type hexaferrites is essential to identify the factors that improve the efficiency of microwave absorbers. In this article, we have examined the characteristics of M-type hexaferrites' microwave absorption. Understanding these materials' magnetic characteristics is essential to comprehending the mechanisms underlying microwave loss. Thus, the magnetic and structural properties of hexaferrites are explored. The different synthesis strategies for these materials are also described because they have a big impact on microwave absorption. Finally, all influential factors identified through previous research are presented, and practical strategies for enhancing the efficiency of absorbers are proposed.

2. Hexaferrites

A type of ferritic minerals with hexagonal crystal structures is known as hexaferrites [55, 56]. Because iron ions are present in their structure, these materials behave magnetically. Blocks of S, R, and T are stacked to form hexaferrites [57, 58]. Fig. 2 shows these blocks in action. M-type, Y-type, W-type, X-type, Z-type, and U-type are the six varieties of hexagonal ferrites [46, 59–62]. Fig. 3 depicts each of these ferrites.

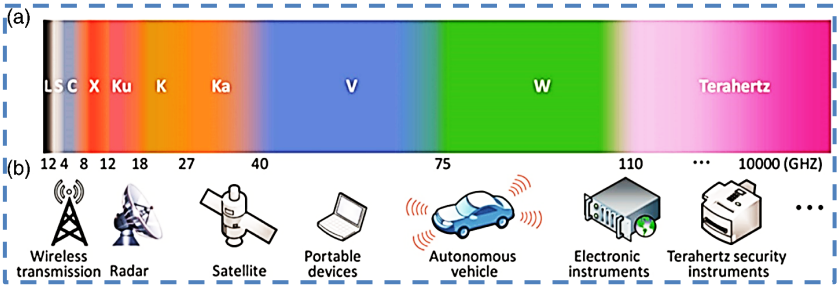

Fig. 1. a) Microwave bands and b) their applications in various fields (reproduced from Ref. [5]).

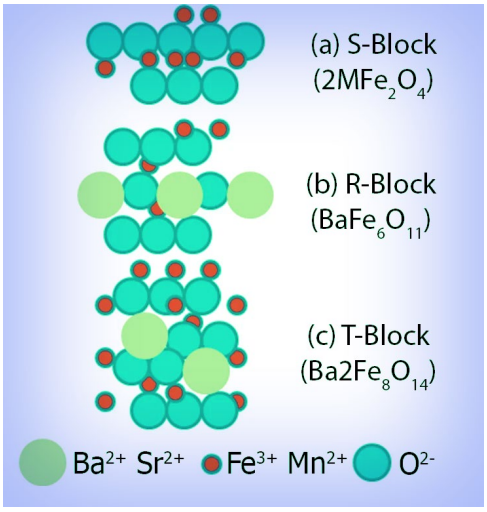

Fig. 2. S, R, and T blocks in hexaferrites (schematic based on Ref. [57]).

Hexaferrites have intricate structures, as the image makes clear [63]. Also, Table 1 lists the blocks' stacking order for creating the various kinds of hexaferrites. According to the table, depending on the type of hexaferrite, a different space group is obtained. Changes in the space group result in significant alterations in the final properties of the hexaferrite.

The crystal structures of different hexaferrites are shown in Fig. 3. As seen in the figure, the crystal structure of hexaferrites becomes progressively more complex. In addition to the structural complexity, synthesizing these materials is also challenging [64–68], as indicated by the phase diagram [69]. However, all hexaferrites are composed of the blocks mentioned in Fig. 2. The stacking arrangement of these blocks is shown in Fig. 3 and summarized in Table 1. U-type hexaferrite has the most complex structure among the hexaferrites, whereas M-type hexaferrite has the simplest structure [37]. The complexity in the structure of hexaferrites is M, Y, W, Z, X, and U, respectively [70, 71]. A triangular bipyramidal site (2b), a tetrahedral site ($4f_2$), and an octahedral site (12k, $4f_1$, 2a) are among the sites that Fe^{3+} ions occupy in M-type hexaferrites [72–75].

The W-type hexaferrite has a structure similar to that of the M-type hexaferrite (Fig. 3a and b). This type of hexaferrite is formed by stacking blocks in the RSSR∗S∗S∗ sequence (* symbol: 180-degree rotation of the block around the c-axis), where the additional S block layer influences its properties [76]. In Y-type and Z-type hexaferrites (Fig. 3c and d) [77], the structure consists of spin blocks L and S, which exhibit large and small magnetic moments along the [001] direction, respectively [78]. The stacking of these spin blocks leads to the emergence of a non-collinear magnetic structure [79]. Fig. 3e presents one-third of the U-type hexaferrite structure. The U- and Z-type hexaferrite can also be described using M- and Y-type blocks [61]. Z-type hexaferrite has a 33-layer structure stacked along the c-axis, with a unit cell containing 140 atoms [80]. The X-type hexaferrite structure is depicted in Fig. 3f [81]. In the structure of X-type hexaferrite, there are three octahedral sites at the boundary between the S-S and S-R blocks, two octahedral sites and one trigonal bipyramidal site in the R block, and one octahedral site and two tetrahedral sites in the S block. The iron ions, by being located in these sites, determine the magnetic behavior of this ferrite [38].

3. M-type hexaferrite

3.1. Methodology of the review

The materials for this review were collected from reputable publishers and scientific databases, including ScienceDirect, Springer, Wiley, and others. The literature search was conducted using relevant keywords such as hexaferrites, M-type hexaferrite, BaM, SrM, PbM, barium hexaferrites, strontium hexaferrites, lead hexaferrites, doped hexaferrites, hexaferrite composites, etc. Priority was given to the most recent publications related to the studied material in order to provide an up-to-date overview.

To avoid redundancy, duplicate or repetitive studies were carefully excluded. The selected articles were analyzed to cover different aspects of the material's properties from multiple perspectives. Finally, based on the reviewed studies, a roadmap was outlined to suggest possible strategies for improving the properties of the material under investigation.

3.2. Structural features

M-type hexaferrites will be the main topic of this essay. The general formula for M-type ferrites is $AFe_{12}O_{19}$, where A denotes metal cations such as strontium (Sr), barium (Ba), and lead (Pb) [33, 85–87]. Phillips was the first to study the magnetic characteristics of this kind of hexaferrite in the 1950s [88–90]. The most well-known M-type hexaferrite is BaM. Initially, this material was referred to as ferroxdure [91]. M-type hexaferrites are considered hard magnetic ferrites [92–95]. While BaM has a lower M_s compared to magnetic alloys, its production is cost-effective. As a result, it is widely used in industry.

Table 1. The combination, chemical formula, stacking order, and space group of different hexaferrites (the 180-degree rotation of the block around the c-axis is indicated by the * symbol) [82–84].

Hexaferrite type	Combination	Chemical formula	Stacking order	Space group
U	2M + Y	$A_4M_2Fe_{36}O_{60}$	RSR∗S∗T∗S∗	R-3m
X	2M + S	$A_2M_2Fe_{28}O_{46}$	RSR∗S∗S∗	R-3m
Z	M + Y	$A_3M_2Fe_{24}O_{41}$	RSTSR∗S∗T∗S∗	$P6_3/mmc$
W	M + S	$AM_2Fe_{16}O_{27}$	RSSR∗S∗S∗	$P6_3/mmc$
Y	Y	$A_2M_2Fe_{12}O_{22}$	TSTSTS	R-3m
M	M	$AFe_{12}O_{19}$	RSR∗S∗	$P6_3/mmc$

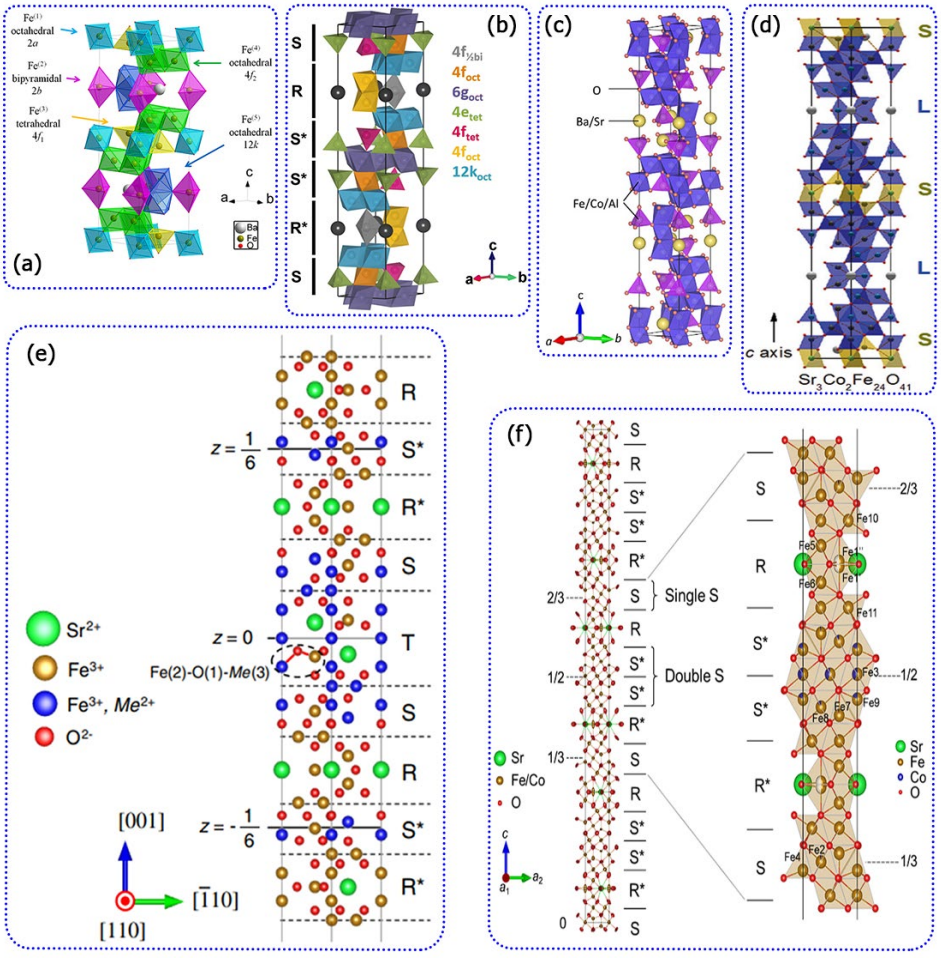

Fig. 3. a) M-type (reproduced from Ref. [75]), b) W-type (reproduced with permission Ref. [76]), c) Y-type (reproduced from Ref. [77]), d) Z-type (reproduced from Ref. [79]), e) U-type (reproduced from Ref. [67]), and f) X-type hexaferrites (reproduced with permission from Ref. [81]).

Additionally, these materials exhibit high electrical resistance [96]. SrM is also one of the most well-known M-type hexaferrites. The strontium ions are smaller than barium ions, which leads to changes in the crystal structure of SrM, resulting in different final properties compared to BaM [91].

M-type hexaferrites have a molecular structure composed of S and R blocks, with the final formula for the unit cell being RSR*S* [97]. The block has turned 180 degrees around the c-axis, as shown by the symbol *. To determine whether ferrite is created, XRD patterns of the samples are prepared. Fig. 4 displays the XRD spectra for PbM, SrM, and BaM. Fig. 4a displays the XRD patterns of doped BaM with different Zn-Sn concentrations [98]. As doping levels rise, the (008) peak's strength falls, suggesting that the hexaferrite structure's degree of orientation is decreasing. Fig. 4b illustrates the XRD patterns of europium (Eu)-doped strontium hexaferrite [99]. It can be observed that substitution occurs with an increase in doping levels up to a certain limit. However, when the doping level exceeds this limit, as shown in the figure, a secondary phase of Fe_2O_3 appears. Additionally, a shift can be observed in the XRD pattern of the samples, which is attributed to the substitution process. Fig. 4c displays the XRD pattern of $Pb_{1-x}Cr_xFe_{12}O_{19}$ [100]. Based on the XRD pattern, the samples exhibit phase purity at different doping levels, and no secondary phases are formed. Substitution in $Pb_{1-x}Cr_xFe_{12}O_{19}$ leads to changes in lattice parameters due to the difference in ionic radius between chromium and lead ions.

The morphology of the samples can be examined using the pictures obtained from SEM. Fig. 5a shows SEM images of BaM sintered at various temperatures and under different atmospheres [75]. The image makes it clear that as the temperature rises, grain size increases. In an N_2 gas environment, excessive sintering has a major impact on grain growth at 1280 °C. Therefore, employing an N_2 gas atmosphere allows for a reduction in the sintering temperature. This occurs because the N_2 atmosphere prevents the formation of secondary phases such as α-Fe_2O_3. Fig. 5b presents SEM images of two types of SrM [101]. In this figure, anisotropic hexaferrites can be clearly distinguished from isotropic ones. Additionally, the anisotropic hexaferrites are arranged in a hexagonal structure. A group was able to synthesize different nanostructures of PbM with different precursors [102]. Using lead acetate, ethylene diamine, lemon juice, and citric acid, the group was able to prepare structures such as nanoplates, nanoparticles, and nanorods, respectively. Furthermore, the amount of precursor used can influence the direction of grain growth.

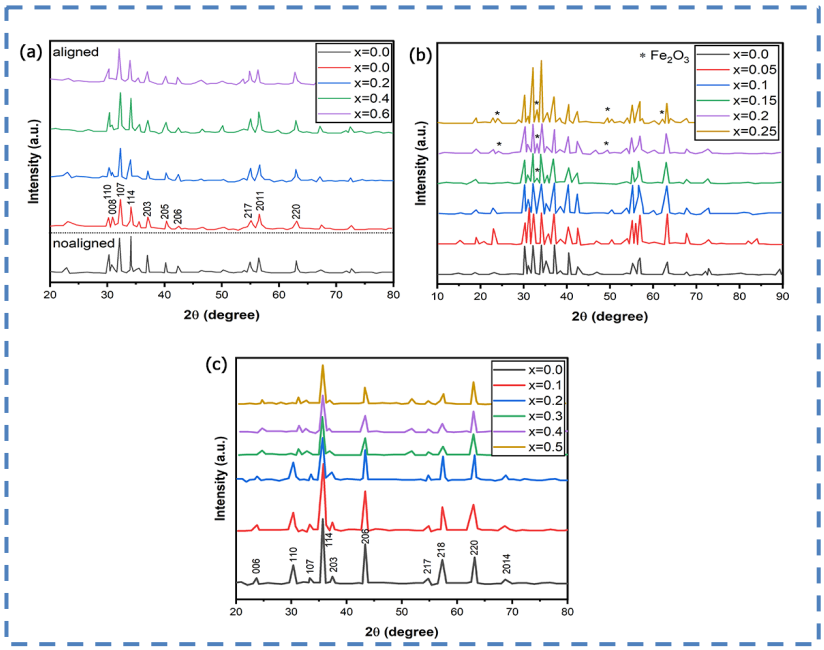

Fig. 4. XRD pattern of a) barium (schematic based on Ref. [98]), b) strontium (schematic based on Ref. [99]), and c) lead hexaferrite (schematic based on Ref. [100]).

3.3. Synthesis of M-type hexaferrites

Although hexaferrites were discovered long ago, their synthesis remains challenging, sensitive, and complex [59, 69]. For instance, as shown in Table 2, heating a mixture of BaO, Fe_2O_3, and CoO results in the formation of different phases at various temperatures. Consequently, precise control of the heating temperature is crucial to obtain the desired phase.

The formation of a single-phase hexaferrite typically requires high temperatures. However, increasing the temperature promotes grain growth, and at elevated temperatures, abnormal grain growth can occur. This phenomenon is undesirable for applications requiring uniformly sized particles. Due to the specific synthesis conditions of hexaferrites, a phase diagram is often developed for these materials. As shown in Fig. 6a, the synthesis conditions for obtaining BaM must be carefully controlled within a narrow region. According to the phase diagram, other types of hexaferrites can also be achieved under specific conditions. In one study, the formation of various phases for synthesizing SrM was investigated at different temperatures and iron contents [103]. The corresponding phase diagram is shown in Fig. 6b. Based on the diagram, as the doping level decreases and the sintering temperature increases, the presence of secondary phases in the composition is reduced.

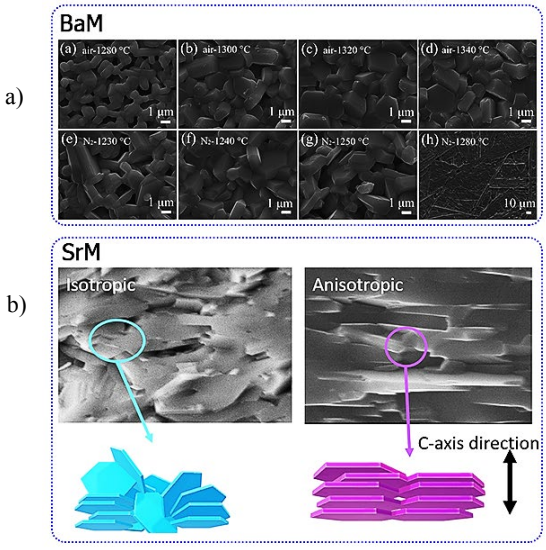

Fig. 5. SEM images of BaM (reproduced from Ref. [75]) and SrM (reproduced from Ref. [101]).

Table 2. Phases formed from the compounds $BaO.Fe_2O_3.CoO$ at different temperatures [91].

Temperature, °C	Major products	Minor products
500	α-Fe_2O_3, Co_3O_4, BaO	-
600	α-Fe_2O_3, Co_3O_4, BaO	$CoFe_2O_4$, $BaFe_2O_4$
700	α-Fe_2O_3, $CoFe_2O_4$, $BaFe_2O_4$	BaM, BaO
800	BaM, $BaFe_2O_4$	α-Fe_2O_3, $CoFe_2O_4$
900	BaM, Y	$BaFe_2O_4$, $CoFe_2O_4$
1000	BaM, Y	$BaFe_2O_4$, $CoFe_2O_4$
1100	Y, BaM	$BaFe_2O_4$, $CoFe_2O_4$
1200	Z, Y, BaM	W
1300	Z	Y, W
1400	W, Z	-

As mentioned earlier, the synthesis of hexaferrites must be conducted under specific conditions to prevent the formation of secondary phases. To enhance the magnetic and microwave absorption properties of hexaferrites, more synthesis methods need to be researched. In recent years, several methods have been employed for hexaferrite synthesis, including the commonly used solid-state reaction [99, 104, 105], co-precipitation [106, 107], sol-gel [108–110], hydrothermal [111, 112], molten-salt [113–115], microemulsion [85, 116, 117] and mechanical alloying [34, 118, 119] methods. In the following sections, we aim to describe the solid-state reaction, co-precipitation, sol-gel, and hydrothermal methods in detail.

3.3.1. Solid-state reaction method

This is the most popular, straightforward, and quick way to make hexaferrites. It is widely employed in the industry for hexaferrite production. The process of this method is illustrated in Fig. 7. As shown, the precursors, including metal oxides and metal salts, are first weighed [104, 120, 121]. The precursors are then mixed in specific weight ratios. Additionally, the precursor mixture can be prepared in an aqueous medium [122]. If necessary, the particle size is reduced and homogenized using a ball milling device [48, 99, 123]. The milling process can be conducted in various media, such as acetone or ethanol [124–126]. Subsequently, the resulting powder is placed in a furnace for sintering [96, 105]. The sintering process can be performed in an atmospheric environment or under other gases such as N_2 gas [75].

3.3.2. Co-precipitation method

Aqueous solution is used to produce the end product in the co-precipitation process, which is a wet chemical technique. The steps of the co-precipitation process are illustrated in Fig. 8 [127]. Precursors such as metal salts are used in this method. After dissolving the precursors in a solvent, a precipitating agent, typically sodium hydroxide [59, 128, 129], is added to the solution. The solvent used can be deionized water or hydrochloric acid [107]. By adjusting the pH of the solution, the final product is obtained after several washing, filtration, and drying steps [130]. To improve the crystalline quality of the samples, calcination may be performed after drying [8, 106]. Finally, to further reduce particle size, the ball milling process is conducted [131]. The final properties of the material are greatly influenced by a number of parameters in this process, including the temperature and time of mixing, the ratio of precursors, the calcination temperature, and the kind and quantity of precipitating agent.

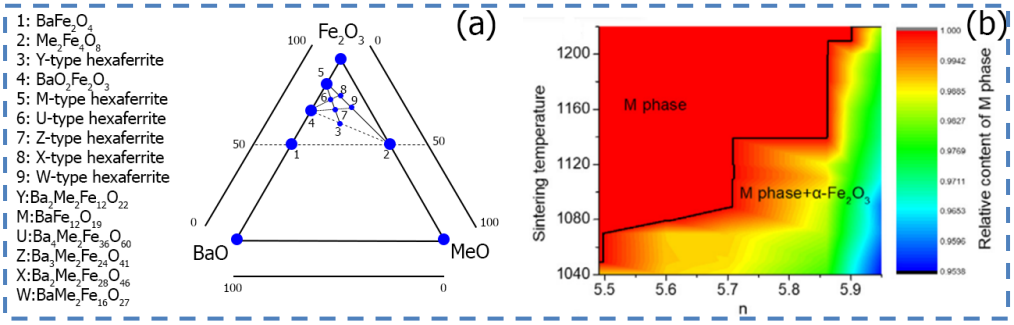

Fig. 6. a) Phase diagram for the formation of phases and different types of hexaferrites (schematic based on Ref. [69]) and b) diagram of the the growth of the SrM phase (reproduced from Ref. [103]).

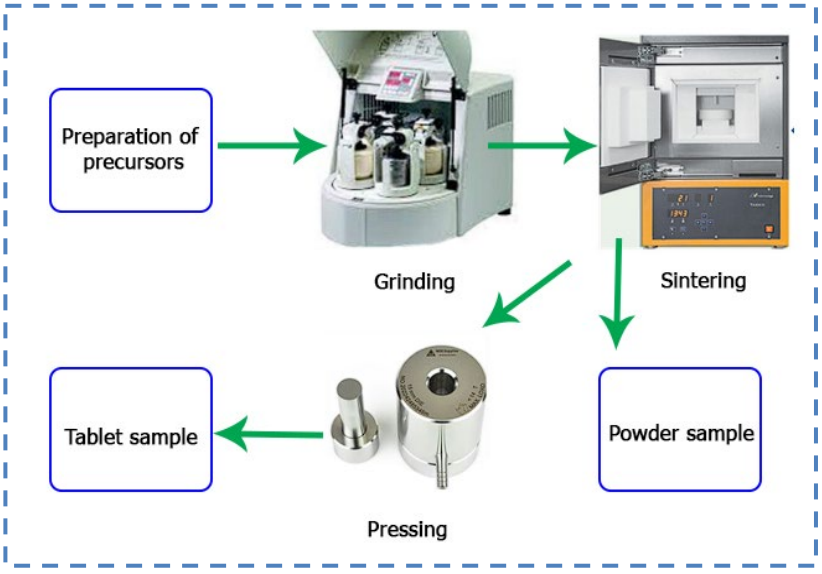

Fig. 7. Solid-state method for the preparation of $BaFe_{10-x}Al_2Mg_xO_{19}$ (schematic based on Ref. [104]).

3.3.3. Sol-gel method

This is one of the most popular methods for creating hexaferrites, along with the solid-state reaction method. Precursor materials, which may be metal-organic or inorganic, are mixed in the sol-gel process [132]. Usually, a certain quantity of tartaric or citric acid is added to the mixture [133, 134]. In order to prevent metal nitrates from precipitating during evaporation, citric acid is utilized [100, 135]. The pH of the solution is then adjusted by adding a precipitating agent [108, 109]. At the colloidal level, a sol is initially formed, which can then be concentrated and heated to produce a gel [136, 137]. The resulting gel is subsequently ignited to produce the final powder. Afterward, washing, drying, and calcination steps are performed to prepare the final product [138–140]. This method produces fine-grained polycrystalline ferrites with a uniform particle size distribution [141]. The sol-gel process is illustrated in Fig. 9. In Ref. [142], after preparing precursor solutions, tomato pulp was used as a fuel.

3.3.4. Hydrothermal method

This method involves reacting precursors in an aqueous solution at high temperature and pressure, typically in a sealed autoclave [143, 144]. Fig. 10 illustrates this process for synthesizing $BaFe_{12}O_{19}$ using the hydrothermal method. In this study, CTAB (cetyltrimethylammonium bromide) was used as a reagent [112]. The hydrothermal process is conducted in a solvent, usually water, which enhances the solubility of the precursors and facilitates better formation of crystalline phases. The choice of precursors for synthesizing hexaferrites in this method can

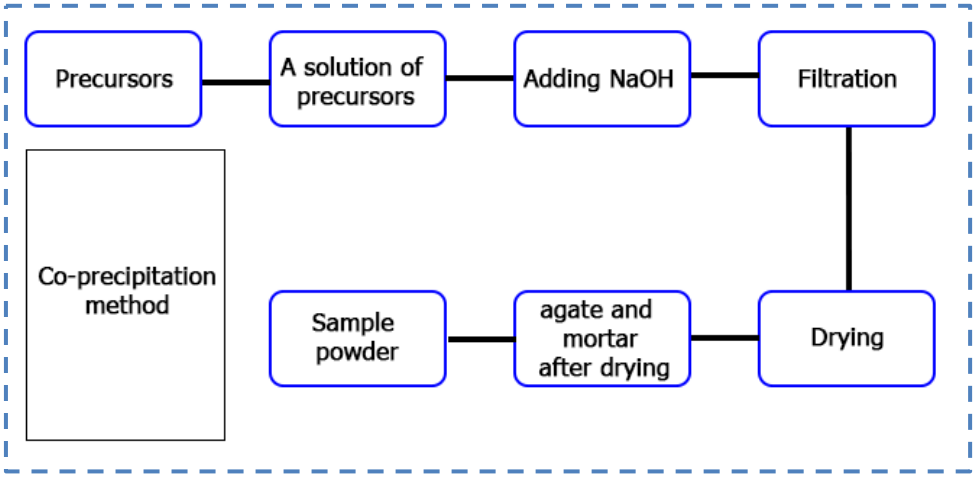

Fig. 8. Co-precipitation method for preparing $Co_{1-x}Mn_xFe_2O_4$ ferrite (schematic based on Ref. [127]).

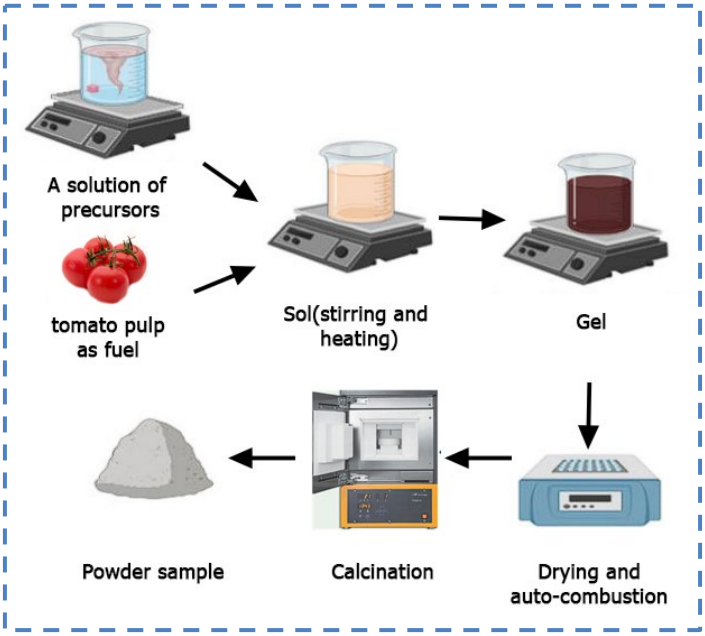

Fig. 9. Synthesis of BaM using the sol-gel method and using tomato pulp as fuel (schematic based on Ref. [142]).

significantly affect the properties of the final product. A precipitating agent is also used in this method to adjust the pH [111, 133, 145]. In the hydrothermal process, nucleation of the hexaferrite phase occurs when the solution becomes supersaturated, and growth of the desired hexaferrite phase begins. This method allows for better control over the size, shape, and crystallinity of the synthesized particles, and due to the uniform distribution of precursors in the solvent, more homogeneous particles can be expected. Additionally, this method is carried out at relatively lower temperatures compared to other methods, which is a significant advantage [146]. Finally, after the reaction in the sealed environment, steps such as washing, drying, and calcination may be necessary to enhance the quality of the samples [147, 148].

3.4. Magnetic properties

Fig. 11 shows the magnetic configuration of M-type hexaferrite [58]. The magnetic moments in the corresponding diagram are as follows: 12k(↑), $4f_2$(↓), and 2a(↓) are found in the octahedral sites; $4f_1$(↓)s are found in the tetrahedral sites; and 2b(↑) is found in the trigonal bipyramidal sites [72–74]. While the ions in the 2a, $4f_1$, and $4f_2$ sites only slightly affect the magnetic anisotropy constant (K_1), the Fe^{3+} ions in the 2b sites significantly affect it. The total magnetic moment (μ_{tot}) is represented as follows [121]:

$$\mu_{tot} = \mu_{2a} + \mu_{2b} - \mu_{4f_1} - \mu_{4f_2} + \mu_{12k} \quad (1)$$

and the magnetic moment at the respective point is indicated by μ_i, where μ_i stands for 2a, 2b, $4f_1$, $4f_2$, and 12k. Consequently, it is simple

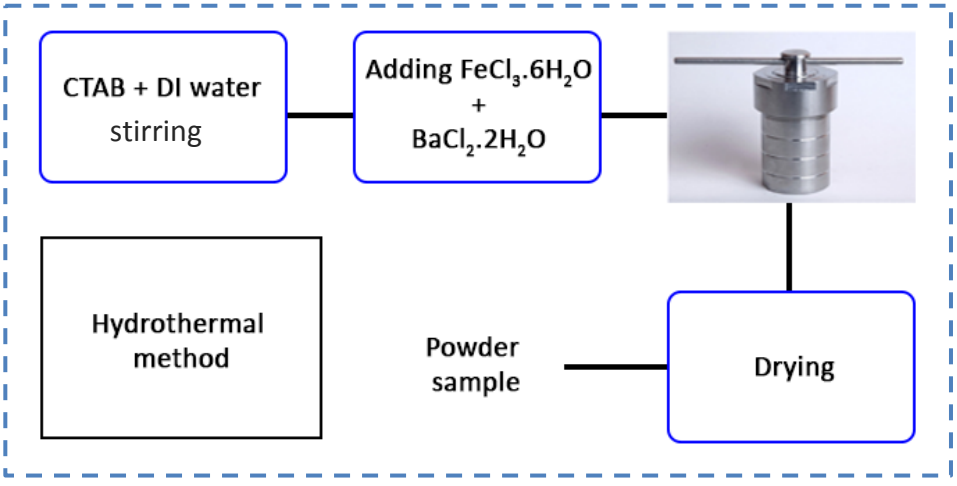

Fig. 10. Synthesis of BaM nanorods by hydrothermal method (reproduced from Ref. [111]).

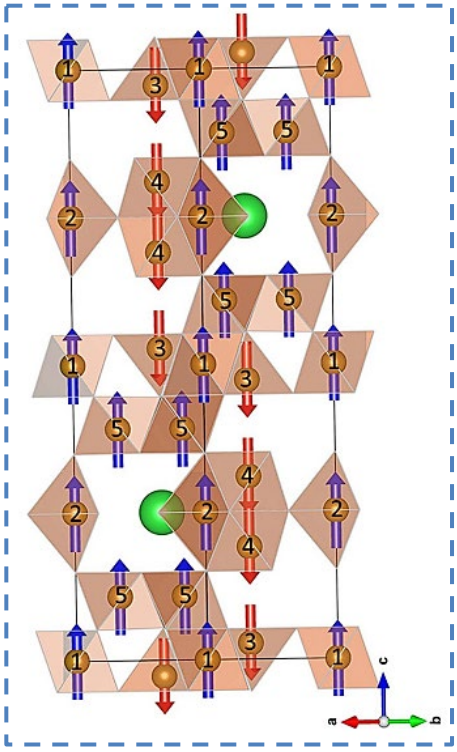

Fig. 11. Spin configuration in M-type hexaferrite; iron ions are numbered (reproduced from Ref. [58]).

to adjust the magnetic characteristics of M-type hexaferrites by replacing Fe^{3+} ions in the lattice with appropriate cations [121]. In the following paragraphs, we will review the magnetic properties studied in recent years. In conclusion, the magnetic behavior of hexaferrites is determined by the arrangement of Fe^{3+} ions in different sites within the structure [149].

Tables 3 and 4 show M_s, H_a, H_c, and m_B for pure, doped, and composites of M-type hexaferrites. According to Table 3, it can be seen that strontium and BaM offer better magnetic properties than PbM. M_s is in the range of 1.3–87.04 emu/g, and the coercivity is in the range of 0.33–6.54 kOe. According to Table 3, it is quite clear that doping of hexaferrites can change their magnetic behavior. Also, the creation of multi-component composites for use in electromagnetic absorbers can weaken the magnetic properties of hexaferrites (Table 4). In the following, we will explain in detail the factors that change the magnetic behavior of hexaferrites due to their doping or combination with other materials.

Hu and his colleagues synthesized BaM using the co-precipitation method [150]. This group investigated the magnetic properties of the material at different precipitation times and calcination temperatures. According to the reported results, all samples exhibited hard magnetic behavior. Additionally, at the lowest calcination temperature (800 °C), a lower H_c was observed compared to higher calcination temperatures. This was explained by the sample's decreased crystallinity at lower calcination temperatures. Higher M_s and M_r were the outcomes of raising the calcination temperature. The sample's decrease in the α-Fe_2O_3 phase and increase in the BaM phase explained for this.

The critical size for a single magnetic domain in BaM has been reported to be 460 nm. Furthermore, if the domain size is smaller than 4 nm, the material becomes superparamagnetic. The nanoparticles synthesized by this group were within the size range of 4–460 nm. H_c in nanoparticles larger than 460 nm significantly decreased due to exchange coupling between particles. In the samples, an increase in nanoparticle size led to a reduction in H_c, which was also attributed to exchange coupling between particles.

Li and his colleagues synthesized BaM using the salt-melt method [114]. The remanent magnetization loop becomes thinner with an increase in calcination temperature starting from 100 °C, meaning that H_c decreases.

Table 3. Magnetic parameters of M-type hexaferrites.

Pure or doped phase	M_s (emu/g)	H_a (kOe)	H_c (kOe)	m_B (μB)	Ref.
$BaFe_{9.95}Al_2Mg_{0.05}O_{19}$	49.95	1.60	4.98	9.41	[104]
$Ba_{0.8}In_{0.2}Fe_{12-x}Tb_xO_{19}$	55.78	1.87	6.00	10.50	[151]
$BaFe_{12}O_{19}$	55.52	-	3.05	-	[142]
$Ba_{0.6}Sr_{0.4}Fe_{9.5}Ce_1Al_{1.5}O_{19}$	44.44	-	6.51	9.43	[126]
$Ba_{0.8}In_{0.2}Fe_{12-x}Ni_xO_{19}$	58.32	1.72	5.51	11.60	[125]
$Ba_{1-x}Nd_xFe_{12-y}Cu_yO_{19}$	68.40	-	5.52	-	[117]
$BaZn_xZr_xFe_{12-2x}O_{19}$	87.04	14.68	4.21	-	[134]
$BaFe_{12}O_{19}$	66.80	18.8	3.50	13.22	[141]
$BaCe_xDy_xFe_{12-2x}O_{19}$	26.30	-	5.75	-	[139]
$Ba_{0.95}Y_{0.05}Fe_{12-x}Mn_xO_{19}$	23.00	-	4.00	-	[123]
$Sr_{1-x}Ca_xFe_{12}O_{19}$	72.63	17.34	5.39	-	[138]
$Sr_{1-x}Sm_xFe_{12}O_{19}$	9.57	-	6.20	-	[149]
$PbCu_xFe_{12x}O_{19}$	25.51	-	0.33	5.40	[131]
$Pb_{1-x}Cr_xFe_{12}O_{19}$	64.00	-	6.54	-	[100]
$Pb_{1-x}Ce_xFe_{12}O_{19}$	26.70	-	3.92	-	[108]

Table 4. Magnetic parameters of M-type hexaferrite composites.

M-type hexaferrite composites	M_s (emu/g)	H_a (kOe)	H_c (kOe)	m_B (μB)	Ref.
Carbon nanotubes (CNTs)/$SrFe_{12}O_{19}$	10.21	-	1.25	-	[22]
Polyacrylonitrile/$SrFe_{12}O_{19}$ (10%)	0.63†	-	2.27	-	[152]
$BaFe_{12}O_{19}$/calcium copper titanate	41.88†	-	3.89	-	[7]
Expanded graphite/$BaFe_{12}O_{19}$ (BF)	36.0†	-	0.11	-	[21]
Expanded graphite/CNTs/BF	42.74†	-	0.19	-	[21]
$BaFe_{12}O_{19}$/multiwalled carbon nanotubes	1.30	-	1.05	-	[147]

† Indicates the normalized M_s values. The M_s value shown is for the magnetic part only.

H_{Ci} of the particles can be determined using the Stoner-Wohlfarth theory, as follows [153]:

$$H_{Ci} = 2K_1 / \mu_0 M_s \quad (2)$$

Using this equation, it is possible to calculate the calcination temperature at which K_1 reaches its maximum value. Li's group [114] reported that decreasing the Fe^{3+}/Ba^{2+} molar ratio maximizes the coercivity. As can be clearly seen from the above equation, in this case, K_1 is at its maximum.

The larger the value of SQR (determined by SQR = M_r/M_s) [154, 155], the more suitable the material is for biomedical applications and recording media. The distribution of particles and their size affect SQR [152]. In this study, the SQR value was found to be 0.55, indicating that the nanoparticles are composed of single magnetic domains. The group also reported that the magnetic energy can vary depending on the sources of Fe ions. Additionally, the type of method used also plays a role in the final magnetic energy.

In another study, Mironovich and his colleagues synthesized BaM and SrM using the hydrothermal method by varying the Fe^{3+}/Ba^{2+} and Fe^{3+}/Sr^{2+} molar ratios in the precursors [144]. In SrM, when the Fe^{3+}/Sr^{2+} ratio was equal to 5, the remanent magnetization loop exhibited a wasp-waist shape. This behavior was attributed to the coexistence of different magnetic phases within the material and the non-uniformity in grain size, which leads to a distribution of coercivity in the sample. The team proposed that the presence of a secondary phase, $SrFeO_{3-x}$, was the cause of the wasp-waist feature's occurrence in this sample. Prior research has demonstrated that the absence of chemical interactions between magnetic phases leads to a wasp-waist remanent loop. Nonetheless, a significant link between the hexaferrite and hematite phases is shown in the common remanent loop. The group also reported observing the wasp-waist remanent loop in BaM with molar ratios of 5 and 7.

Gholizadeh and colleagues synthesized $Sr_{1-x}Ca_xFe_{12-x}Gd_xO_{19}$ hexaferrites [60]. The wasp-waist hysteresis loop observed in their study was attributed to the coexistence of magnetic phases, dipole-dipole interactions between single-domain nanoparticles, and a bimodal grain size distribution. They demonstrated that increasing the Ca-Gd substitution enhances the magnetic moment. On the other hand, M_s is reduced when Ca^{2+} ions are added to SrM. At the 2b location, the closest neighbors of Sr^{2+} ions are Fe^{3+} ions, which are 0.340 nm apart. The structure experiences strain when Ca^{2+} ions are substituted at the Sr^{2+} site, breaking the lattice symmetry surrounding the 2b site. M_s decreases as a result of the resultant strain weakening the Fe–O–Fe connections.

The strongest exchange interaction occurs between the $4f_2$ (↓) and 12k(↑) sites, where the Fe–O bond length and angle are the shortest and largest, respectively, compared to other sites. Conversely, the interaction between the 12k(↑)–12k(↑) sites is the weakest.

The total anisotropy energy ($K_{eff}V$) can be defined as follows [60]:

$$K_{eff}V = E_{shape} + E_{surface} + E_{ME} + E_{MC} \quad (3)$$

The total effective field H_c can be calculated as follows [156]:

$$H_c = a\left(\frac{2K_1}{M_s} - N_d M_s\right) = a(H_a - H_d) \quad (4)$$

In the above equation, a is a constant, H_d is the anisotropic field coefficient for shape magnetization, and N_d is the shape magnetization demagnetization coefficient. In this study, when the level of Ca^{2+}/Gd^{3+} doping is low, the contribution of the first term is greater than that of the second term. However, as the doping level increases, N_d rises, and the contribution of the second term dominates over the first term, leading to a reduction in coercivity in the sample with a doping level of x = 0.20.

A group doped SrM with Eu–Co ions [157]. The octahedral $4f_2$ site features a low-spin structure, where cobalt ions take the place of iron ions. Compared to Fe^{3+} ions, Co^{2+} ions have fewer unpaired electrons. As a result, up to a doping level of x = 0.2, there are more unpaired electrons with high-spin states, which raises M_r and M_s. Magnetic characteristics in hexaferrites are caused by the super-exchange interaction between ions (Fe^{3+}–O^{2-}–Fe^{3+}) [158]. As the super-exchange connection between Fe^{3+}–O–Fe^{3+} weakens above this doping level, M_s falls. As doping levels rise, coercivity likewise falls. According to the group, the $4f_2$ site weakens coercivity by having a detrimental effect on K_1. Single magnetic domains are present in the sample if the SQR is higher than 0.5 [159]. On the other hand, several magnetic domains are present if the SQR is less than 0.5 [124, 160].

A group led by Qin et al. successfully synthesized SrM with varying amounts of iron ions using the conventional ceramic method [103]. The M–H curve obtained at 300 K with an applied magnetic field range of 0–50 kOe is displayed in Fig. 12a. The M–H curve fitted to the Stoner-Wohlfarth model using the law of approach to saturation is shown in Fig. 12b. The following equation can be used to calculate the M_s using this model [161]:

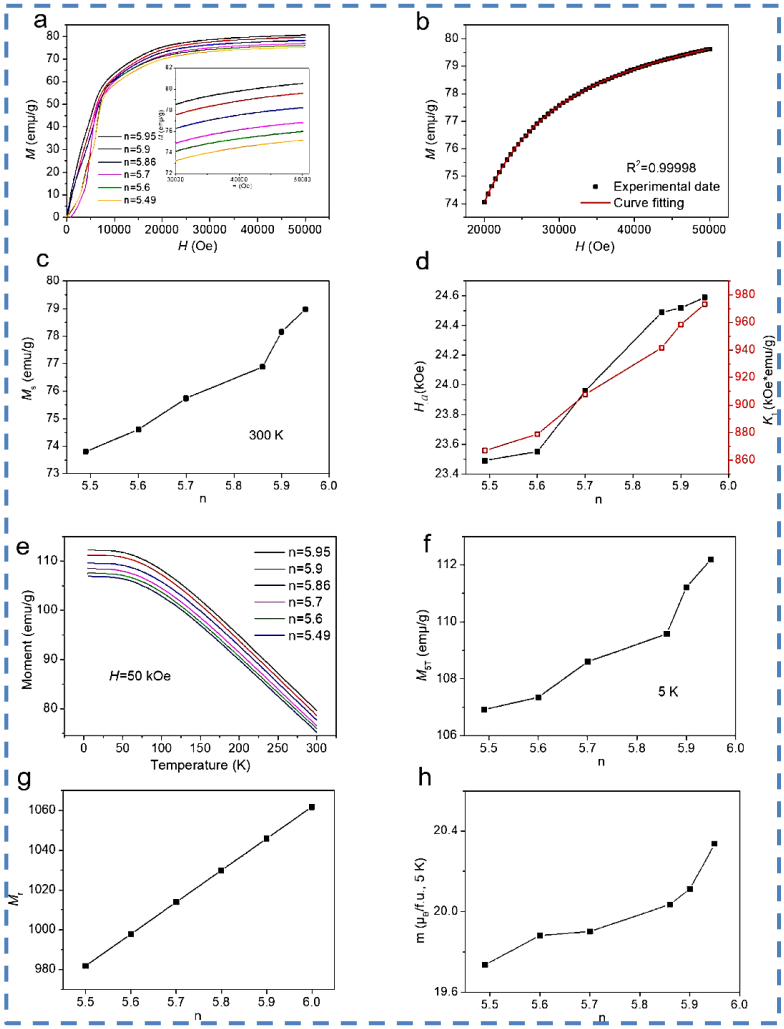

Fig. 12. a) Magnetization curve of $SrO.nFe_2O_3$, $5.49 \leq n \leq 5.95$, b) experimental and fitting results for n = 5.95, c) variations of M_s with iron ion content, d) H_a and K_1, e) M-T curve, f) magnetization at 5 K, g) relative molar mass at different values of n, and h) net magnetic moment calculated based on magnetization at 5 K (reproduced from Ref. [103]).

$$M = M_s\left(1+\frac{A}{H}+\frac{B}{H^2}+\frac{C}{H^3}\right)+\chi_p H \quad (5)$$

In the above equation, A represents inhomogeneity and vanishes at high field, B/H^2 and C/H^3 represent anisotropy, and $\chi_p H$ represents the high-field susceptibility. B and C can be expressed for the hexagonal structure with randomly oriented single-domain particles as follows [103, 161, 162]:

$$B = -\frac{H_a^2}{15} = -\frac{4K_1^2}{15M_s^2} \quad (6)$$

$$C = \frac{2}{105}H_a^3 \quad (7)$$

According to Fig. 12d, both K_1 and H_a decrease with a reduction in molar mass. This is due to the decreased occupation of Fe^{3+} ions in the 2a, 12k, and $4f_1$ sites. Additionally, the bond angle between the $4f_1$ site and the $4f_1$ site decreases, and the bond length at the $4f_1$ site increases.

It can be shown in Fig. 12c that M_s rises in tandem with the iron content. The contribution of iron ions at the 2a, 12k, and 4f1 sites is what causes the drop in M_s with decreasing iron levels. Among these sites, the most significant reduction occurs at the 2a site. This group also reported that when n exceeds 5.6, Fe^{2+} ions occupy the 2a sites, leading to a reduction in the net magnetic moments.

In Fig. 12e, the M–T curve is presented. m_B can be calculated using the following equation [163–165]:

$$m_B = \frac{MM_s}{5585} \quad (8)$$

In the above equation, M represents the molar mass. Based on the calculations, this group reported that with an increase in the molar mass of iron, the net magnetic moment also increases.

Also, theoretically, the magnetic moment of BaM can be calculated as follows [166]:

$$m_B = \left[M_B(12k+2b+2a) - M_A(4f_1+4f_2)\right]\times\mu_B\left(Fe^{3+}\right) \quad (9)$$

Therefore, the total magnetic moment of BaM is:

$$\mu_{tot} = \left(\left[6+1+1\right]\uparrow - \left[2+2\right]\downarrow\right)\times 5\mu_B = 20\mu_B \quad [167] \quad (10)$$

An additional investigation into PbM's magnetic characteristics was carried out [168]. Pb^{2+} (12 nm) and Fe^{3+} (6.4 nm) have different ionic

radii. Local strain brought about by the presence of Pb ions in the structure causes disorder in the lattice and alters the material's magnetic characteristics. Lead and iron have different ionic radii, which changes the lattice size and, consequently, the crystalline magnetic anisotropy. Pb ions can occupy the positions of iron ions, and this results in a weakening of M_s. Iron ions have a slow diffusion rate and exhibit low solubility in type M hexaferrites. This low solubility causes a decrease in the overall magnetic moment. The group attributes M_s to the composition and microstructure of the hexaferrites. A deficiency of iron disrupts the exchange coupling and leads to a decrease in M_s. With the increased substitution of Pb ions in the structure, coercivity increases, which may be due to an increase in grain size and an enhancement in crystalline magnetic anisotropy. The critical domain diameter is defined as follows [168]:

$$D_c = \frac{1.4 W_p}{M_s^2} \quad (11)$$

$$W_p = \left(2K_b T_c K_1 / a\right)^{1/2} \quad (12)$$

In the above equation, a (cm) is the lattice constant. The group reported that the critical domain diameter is larger than the crystallite size, which is the reason for the high coercivity. In this study, the coercivity for x = 0.25, one-quarter of pure PbM, was found. The deficiency of iron is the cause of this phenomenon. The SQR varies from 0.58 to 0.73, indicating the single-domain nature of the samples.

Lanthanum-doped SrM was synthesized by a team under Dai's leadership [169]. According to the group, certain Fe^{3+} ions are changed into Fe^{2+} when La is substituted in the structure. The low-spin 2a sites are preferentially occupied by these Fe^{2+} ions. The exchange contact between the 2b and 12k sites and neighboring lattice points is strengthened because Fe^{2+} has fewer Bohr magnetons than Fe^{3+}. Consequently, M_s. rises. Nevertheless, the exchange contact between the tetrahedral and octahedral sites is diminished when the doping level rises and the Fe^{3+} ions in the 2a sites fall. Some Fe^{3+} ions in the octahedral positions experience a weakening of their high-spin states as a result. In the end, this leads to a decline in M_s. Additionally, the increase in the Fe_2O_3 phase also weakens M_s.

In 2023, Li and colleagues prepared a BaM doped with praseodymium-aluminum [156]. Results obtained from a VSM device indicate that the samples are ferromagnetic. At room temperature, the samples exhibited 30 kOe of coercivity. This team used the M_s saturation approximation method to determine K_1 and H_a. M_s dropped as the concentration of aluminum doping hit 0.1. They propose that the super-exchange interaction between Fe^{3+}–O–Fe^{3+} or variations in the ultra-fine field in the 12k and 2b sites are responsible for the changes in M_s. At the 12k and 2b locations, Al^{3+} ions take the place of Fe^{3+} ions in this structure. With aluminum substitution, the super-exchange interaction weakens, which in turn reduces M_s. Moreover, excessive doping results in the placement of aluminum ions at the grain boundaries, which prevents the grains from growing uniformly and disrupts the structure and homogeneity, ultimately leading to a decrease in M_s. The SQR values of the samples were less than 0.5, indicating that the samples have a multi-domain structure. According to this group, the changes in coercivity can be attributed to grain shape, microstructure, crystallographic magnetic anisotropy, and magnetostriction. In this composition, as the doping level increases, the grain size decreases, which increases the surface-to-volume ratio, enhancing the exchange interaction at the interfaces. Also, the placement of aluminum ions at high doping levels at the grain boundaries reduces domain wall motion. According to Eq. 4, with increasing doping, this group reported that no changes in the shape of the samples occur. Therefore, N_d remains constant. As a result, H_d is the main factor determining the coercivity.

Another group synthesized $Ba(ZnSn)_xFe_{12-2x}O_{19}$ hexaferrite using a ceramic method [98]. They showed that M_r/M_s (perpendicular: 0.81) > M_r/M_s (non-aligned: 0.51) > M_r/M_s (parallel: 0.31), indicating that the sample exhibits anisotropic properties. The easy magnetic axis is perpendicular to the sample's plane, whereas the hard magnetic axis is in the sample's plane. M_s parallel to the plane was lower than that perpendicular to the sample's plane. Due to the presence of anisotropy, M_s along the hard axis is more difficult. The group reported that higher sintering temperatures lead to better and more complete grain formation, which increases the magnetic moments and their alignment. The contact between the grain surfaces and the friction of surrounding crystals determines the resistance to the rotation of the crystallites. A lower SQR was obtained at 1300 °C, which the group attributed to particle agglomeration. Increasing the Zn-Sn doping narrowed the hysteresis loops, suggesting that doping weakens the magnetic moments of the crystallites.

In another study, it was reported that the coercivity increases with sintering temperature up to 1300 °C, but beyond this temperature, coercivity decreases [170]. This phenomenon is attributed to the formation of multi-domain grains. At higher temperatures, Fe_3O_4 also begins to appear. When the amount of Fe_3O_4 increases, M_s increases because the M_s of Fe_3O_4 is higher than that of aluminum-doped barium hexaferrite. According to the relationship between M_s and the critical domain size, the decrease in M_s with aluminum substitution leads to a reduction in K_1, which increases the critical domain size. However, this relationship does not take into account the grain shape and the intergranular interactions.

A group prepared BaM doped with In^{3+} ions [48]. Fig. 13a shows the M–H curve for the samples with different doping levels. As seen in the figure, M_s decreases with increasing doping amount. Doping with larger ions like In^{3+}, unlike smaller ions, shifts BaM from a hard magnet to a soft magnet, reducing the coercivity. The value of K_1 also decreased with increasing doping amount, but this decrease was particularly rapid up to x = 1.8. The group concluded that this sharp decrease occurs due to gradual substitution at the $4f_2$ sites. This result indicates that the exchange pairs corresponding to the $4f_1$ and $4f_2$ sites are weakened. Thus, doping can disrupt the linear magnetic structure of BaM, which is based on strong antiferromagnetic interactions. The antiferromagnetic interaction in BaM can be modeled as follows: Fe^{3+}(2b)-O^{2-}-Fe^{3+}($4f_2$), Fe^{3+}(12k)-O^{2-}-Fe^{3+}($4f_2$), Fe^{3+}(12k)-O^{2-}-Fe^{3+}($4f_1$), and Fe^{3+}(2a)-O^{2-}-Fe^{3+}($4f_1$) triads.

Fig. 13b below shows the magnetic domain pattern of doped BaM. According to the figure, pure BaM has larger magnetic domains that interact with each other. However, as the doping level increases, the domains gradually become smaller and the interactions weaken. The black areas, indicated by white circles, represent the nano-scale magnetic domains that appear in the structure with increasing doping. These domains lead to a decrease in coercivity and M_s.

However, another group prepared $Ba_{1-x}Ce_xFe_{12-x}Zn_xO_{19}$ nanoparticles [171]. They reported that with increasing doping levels up to a certain value, the Ha and M_s increase. This is because, at low doping levels, the substitution of rare earth elements for barium ions pushes the Fe^{3+} ions closer together. After all, rare earth elements have a lower ionic radius than Ba^{2+}. The super-exchange contact is thereby reinforced.

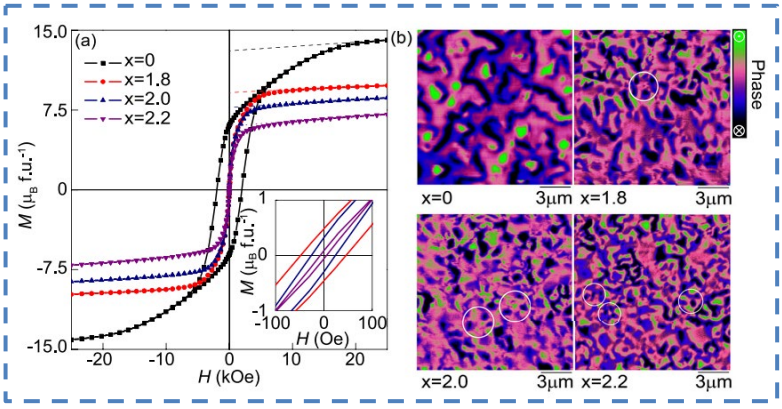

Fig. 13. a) M–H curve and b) magnetic force microscope images of In-doped barium hexaferrite (reproduced from Ref. [48]).

Wu and colleagues prepared two types of compositions [121]. The first type was the preparation of copper and scandium-doped hexaferrite ($BaSc_{0.5}Cu_{0.56}Fe_{10.94}O_{19-\delta}$) using a ceramic method. The second type involved combining the hexaferrite $BaSc_{0.5}Fe_{11.5}O_{19}$ with different weight percentages of CuO and subjecting them to sintering. With the increase in the weight percentage of CuO, M_s initially increases. This is because Cu^{2+} ions have replaced Fe^{3+} ions at the $4f_2$ (low-spin) and 2b (high-spin) sites. Compared to Fe^{3+} ions, Cu^{2+} ions have a lower magnetic moment. Eq. 1 states that this replacement causes M_s to rise. However, as the doping amount increases, a decrease in M_s occurs, which is due to spin canting. Spin canting prevents the regular alignment of spins. Oxygen vacancies have the ability to decrease M_s and weaken the super-exchange interaction. As the weight proportion of CuO as a reactant rises, so does the coercivity. Porosity, impurities, stress, and anisotropy lead to an irreversible magnetic process. Impurities resist domain wall displacement and cause an increase in coercivity.

In Fig. 14a–d, the concentration of Cu^{2+} ions within and at the grain boundaries is shown. The concentration of Cu^{2+} ions at the grain boundaries is higher in the sample where CuO was used as an additive than inside the grains. This phenomenon hinders the displacement of magnetic domain walls through the pinning effect, thereby increasing coercivity.

This group reported that the coercivity in the sample where CuO was used as a reactant was lower than in the sample where CuO was used as an additive. The reason for this difference is illustrated by the distribution of Cu^{2+} ion concentrations in the figures below. Changes in sample preparation led to different Cu^{2+} ion diffusion within the grains, as shown in Fig. 14e. Furthermore, the group reported that the grain size was larger than the critical domain size. In this case, the grain size has an inverse relationship with coercivity. Therefore, the pinning effect and smaller grain size result in higher coercivity when CuO is used as an additive.

3.5. Microwave absorption features

For a microwave absorber to exhibit improved performance, it must achieve good reflection loss and impedance matching. RL is a parameter used in wireless communication to measure the reflection of incident electromagnetic waves from the surface of a material. This parameter is defined using transmission line theory as follows [172, 173]:

$$RL = 20\log\left|\frac{Z_{in} - Z_0}{Z_{in} + Z_0}\right| \quad (13)$$

In the above equation, Z_{in} varies depending on the material. Better impedance matching results in less reflection loss, the closer the input impedance is to Z_0. Z_{in} is defined by the following equation [174, 175]:

$$Z_{in} = Z_0\sqrt{\frac{\mu_r}{\varepsilon_r}}\tanh\left(j\frac{2\pi fd}{c}\sqrt{\mu_r\varepsilon_r}\right) \quad (14)$$

The numbers f and d stand for incident wave frequency and sample thickness, respectively. The imaginary unit is j, while the speed of light is represented by c. In order to ensure that almost the entire incident wave is absorbed into the material, impedance matching is measured as Z_{in}/Z_0. The closer this value is to 1, the better the impedance matching. According to Eq. 14, impedance matching occurs when there is synergy between ε_r and μ_r. In Eq. 14, ε_r and μ_r represent the behavior of a material in electric and magnetic fields, respectively. These two parameters are defined as follows [176, 177]:

$$\varepsilon_r = \varepsilon' - j\varepsilon'' \quad (15)$$

$$\mu_r = \mu' - j\mu'' \quad (16)$$

The real and imaginary parts of ε_r and μ_r represent the storage and dissipation of electromagnetic energy, respectively. The mechanisms responsible for losses in the permittivity component include conduction loss, dipolar polarization loss, ionic polarization, electronic polarization, interfacial polarization, resonance, electron hopping loss, and wave scattering loss.

On the other hand, the mechanisms contributing to losses in the permeability component include hysteresis loop loss, eddy current loss, magnetic resonance, magnetic domain wall displacement, and spin rotation. These mechanisms can attenuate electromagnetic waves. Therefore, to enhance microwave absorption, synergy between dielectric and magnetic losses must occur to minimize reflection loss.

The dielectric and magnetic losses in each component can be calculated using the following equations [176, 178, 179]:

$$\tan\delta_e = \frac{\varepsilon''}{\varepsilon'} \quad (17)$$

$$\tan\delta_m = \frac{\mu''}{\mu'} \quad (18)$$

The higher the values of these two parameters, the lower the reflection loss will be.

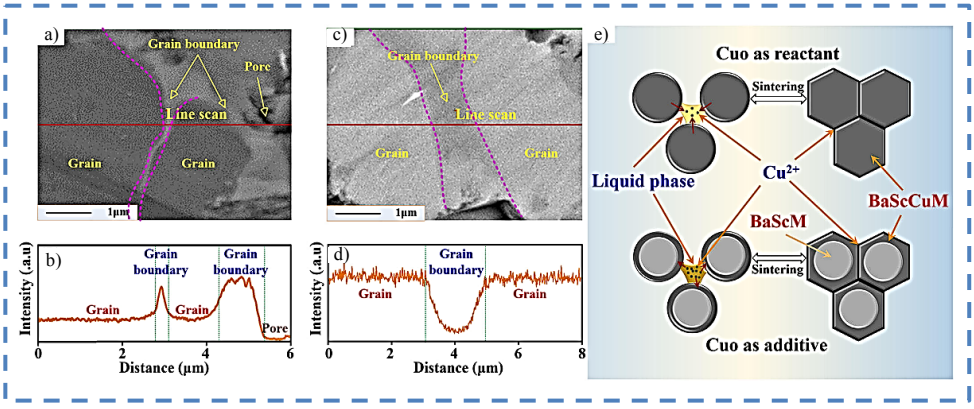

Fig. 14. a, c) SEM images, b, d) Cu^{2+} ion concentration gradients for $BaSc_{0.5}Fe_{11.5}O_{19}$ + 4 wt% CuO and $BaSc_{0.5}Cu_{0.56}Fe_{10.94}O_{19-\delta}$, respectively; and e) schematic of Cu^{2+} ion diffusion in the structure (reproduced from Ref. [121]).

In addition to reflection loss, another parameter called α provides information about the attenuation of the electromagnetic wave. This parameter is defined as follows [172, 180]:

$$\alpha = \pi f / c[2(\mu''\varepsilon'' - \mu'\varepsilon') + 2[(\mu''\varepsilon'' - \mu'\varepsilon')^2 + (\mu'\varepsilon'' + \mu''\varepsilon')^2]^{1/2}]^{1/2} \quad (19)$$

According to the above equation, the higher the attenuation constant and the better the impedance matching, the greater the absorption will occur.

Based on Eq. 14, the input impedance is dependent on the thickness. To achieve the optimal thickness for d_m, the following equation can be used [181, 182]:

$$d_m = \frac{nc}{4f_m\sqrt{|\varepsilon_r||\mu_r|}} \quad (n = 1,\ 3,\ 5,\ \ldots) \quad (20)$$

In the above equation, f_m is directly related to the matching thickness, and the optimal thickness can be determined using this relationship.

Polarization in the material occurs due to the Debye relaxation process. In this process, when an alternating electromagnetic field is applied, the polarization in the material cannot immediately align with the applied field. However, after a delay period, the dipoles reach equilibrium. The relaxation process of polarization can be studied using the Cole-Cole equation [183–185]:

$$\left(\varepsilon' - \frac{\varepsilon_s + \varepsilon_\infty}{2}\right)^2 + (\varepsilon'')^2 = \left(\frac{\varepsilon_s - \varepsilon_\infty}{2}\right)^2 \quad (21)$$

Using the above equation, the relaxation processes resulting from various types of polarization in the material can be identified. The real and imaginary parts of ε_r can be defined as follows [183]:

$$\varepsilon' = \varepsilon_\infty + \frac{\varepsilon_s - \varepsilon_\infty}{1 + \omega^2\tau^2} \quad (22)$$

$$\varepsilon'' = \frac{\varepsilon_s - \varepsilon_\infty}{1 + \omega^2\tau^2}\omega\tau + \frac{\sigma}{\omega\varepsilon_0} \quad (23)$$

where σ represents conductivity.

f_r for polycrystalline hexaferrites can also be expressed as follows [74]:

$$f_r = \gamma\frac{2K}{M_s} = \gamma\frac{H_a}{2\pi} \quad (24)$$

In this equation, γ represents the gyromagnetic ratio. From the above equation, it can be seen that H_a is proportional to the resonance frequency. Additionally, H_a is related to the magnetic permeability. As a result, by adjusting the permeability, the resonance frequency can be shifted. On the other hand, the imaginary part of permeability is defined as follows [74]:

$$\mu'' = \frac{M_s}{2\alpha H_a} \quad (25)$$

In the above equation, H_a is given by the following relation [186, 187]:

$$H_a = \frac{2K_{eff}}{M_s} \quad (26)$$

where K_{eff} is the effective anisotropy constant. By combining the three above equations, the following relation can be derived:

$$\mu'' = \frac{\gamma M_s}{4\pi\alpha f_r} \quad (27)$$

According to this relationship, the frequency has a direct relationship with M_s but an inverse relationship with the imaginary component of permeability. Because the imaginary part of permeability increases with increasing M_s, the magnetic loss increases as well. This occurs because, as M_s increases, H_a decreases according to the relation. When H_a decreases, the magnetic moments can oscillate more freely in different directions. As the distribution of oscillations increases, energy loss also increases. Consequently, the reflection loss will rise. Additionally, with various orientations of magnetic moments, absorption will occur over a broader frequency range, contributing to an increase in the absorption bandwidth.

The loss due to eddy currents can be determined using the following equation [181, 183]:

$$C_0 = \mu''(\mu')^{-2}f^{-1} = 2\pi\sigma d^2\mu_0 \quad (28)$$

where σ is the conductivity. According to the aforementioned connection, if the magnetic losses are solely due to eddy current losses, the value of μ_0 should remain constant with respect to frequency.

Now that all the relations influencing the microwave absorption parameters have been introduced, we will review the recent studies conducted by researchers on M-type hexaferrites.

A group synthesized BaM nanoplates by modifying the synthesis method and succeeded in improving the reflection loss [188]. In this study, the microwave absorption parameters of M-type hexaferrites, prepared using various methods, were compared with those obtained by their own method. This group used a combined sol-gel and salt-melt

method to enhance the final structure. In contrast to techniques like co-precipitation, sol-gel, and reverse microemulsion, the results demonstrate that this strategy produces superior reflection loss. The samples' high surface-to-volume ratio improved absorption and increased dispersion. This high surface-to-volume ratio also contributes to the development of dipoles at the surface, which raises the polarization-related loss.

In our previous work, we doped BaM with various elements [189]. The composition $BaMg_{0.9}Zn_{0.9}Zr_{1.8}Fe_{8.4}O_{19}$ exhibited the highest absorption. In this composition, magnesium, zinc, and zirconium ions replace the iron ions in the structure. The increase in absorption was attributed to the reduction of H_a, the decrease in H_c, and, consequently, the increase in permeability. It was also found that the magnetic loss was due to the movement of the domain walls.

In a recent research, a group synthesized the doped hexaferrite $BaFe_{12-2x}(Mn_{0.5}Co_{0.5}Ti)_xO_{19}$ using the solid-state reaction method [190]. They reported that by examining the permittivity parameters, it was found that dielectric resonance dominates the dielectric relaxation process in the samples, resulting in multiple peaks at different frequencies. This phenomenon can be detected using the Lorentz scattering law. This phenomenon can be detected using the Lorentz scattering law. Measurements revealed that both the real and imaginary components of permittivity exhibit several peaks across various frequency ranges, indicating the presence of dielectric resonance. Furthermore, plotting ε″ against ε′ demonstrated that the samples form multiple complete circles rather than semicircles, which is another signature of dielectric resonance. The radius of these circles increases with increasing frequency. As the frequency increases, the radius of these circles also increases. The group attributed dielectric resonance to electron hopping between Fe^{3+} and Fe^{2+} ions [191]. Therefore, the dielectric loss in these samples results from electron exchange between the mentioned sites, leading to surface polarization and intrinsic dipolar polarization [137]. On the other hand, the increase in Fe^{2+} ions in the structure enhances the permittivity [192].

Wang and his colleagues synthesized the hexaferrite $Ba_{0.5}Sr_{0.5}Fe_{12}O_{19}$ doped with lead ions [122]. The dielectric constant showed a high value, which was related to the grain boundaries. During the electron exchange process between Fe^{2+} and Fe^{3+} ions, electrons must pass through the grain boundaries, but these grain boundaries have high resistance. The dielectric constant rises as a result of electron accumulation at the surface and the creation of space charge polarization. The group asserted that different dipoles are formed when ions with different valences are present. Dielectric loss results from a phase delay in the oscillation of these dipoles in the material.

In another study, Darwish and his colleagues synthesized BaM doped with zirconium [105]. As the frequency increases, the permittivity's real portion falls. This occurs because electrons have ample time to align with the applied field at lower frequencies. The electrons can no longer swiftly adjust to the shifting applied field as the frequency rises, though. Polarization thus declines. Further contributing to the decrease in polarization are the constant direction changes that electrons undergo at higher frequencies.

Cobalt-doped SrM was produced by Nguyen et al., who also examined its microwave absorption characteristics [193]. Changes in the real and imaginary components of permeability are associated with magnetic loss in the material, which is caused by the reaction of electron spins and magnetic moments to the applied field. Magnetic loss in ferrites is caused by domain wall resonance and natural resonance. Domain wall resonance typically appears at frequencies below 2 GHz. At higher frequencies, in samples with x = 0.4 and 1, the peaks observed are attributed to spin rotation, which leads to ferromagnetic resonance. Ferromagnetic resonance is dependent on H_c. In the sample with x = 0.1, ferromagnetic resonance occurs at higher frequencies, but as the doping level increases, the peak associated with ferromagnetic resonance shifts towards lower frequencies. The figure also shows that ε" becomes negative at certain frequencies, indicating magnetoelectric coupling in the hexaferrite. It should be noted that in $SrFe_{12-x}Co_xO_{19}$, electron hopping occurs between Fe^{3+}, Fe^{2+}, and Co^{2+} ions.

In the frequency range of 17–18 GHz, the real component of the permittivity in the sample $BaFe_{11.7}(GdAlCo)_{0.1}O_{19}$ approaches one, according to a group headed by Liao et al. [143]. This might be because doping with cobalt ions causes Fe^{3+} to change into Fe^{2+}. The scientists also observed that the strong crystalline magnetic anisotropy of $BaFe_{11.1}(GdAlCo)_{0.3}O_{19}$ is associated with the value $\mu' \approx 1$. A drop in μ′ results from the rise in eddy current and residual loop losses. Due to eddy currents, the sample with doping x = 0.3 in this investigation displayed a decrease in the actual component of permeability. However, by raising the doping level in the $BaFe_{12-3x}(GdAlCo)_xO_{19}$ sample (x = 0.0, 0.1, 0.2, 0.3, and 0.4), the imaginary portion of permeability increased, which is advantageous for microwave absorption.

In 2019, a group synthesized a composite consisting of BaM and calcium copper titanate [7]. Based on the results obtained, it was found that the skin effect can reduce both the real and imaginary parts of permeability due to eddy current losses. The resonance peaks in magnetic losses may be attributed to particle size, spin wave excitation, and surface effects. This group also confirmed eddy current losses at lower frequencies and exchange resonance losses in the 16–17 GHz frequency range.

In another study, a nanocomposite consisting of carbon nanotubes and $BaCu_xMg_xZr_{2x}Fe_{12-4x}O_{19}$ was prepared by Nikmanesh and colleagues [8]. They observed that without the addition of carbon nanotubes, the real and imaginary parts of the permeability of BaM were low. Carbon nanotubes, dispersed throughout the composite, enhance its conductivity. The change in the frequency of ferromagnetic resonance with the applied magnetic field is explained by ferromagnetic resonance theory. According to Eq. 24, the resonance frequency has a positive correlation with H_a, which in turn has a direct relationship with magnetization. Therefore, the applied magnetic field influences the ferromagnetic resonance frequency. This group succeeded in achieving a reflective loss of -23.1 dB with an effective bandwidth of 6 GHz by doping BaM and combining it with carbon nanotubes.

Another study found that doping BaM with bismuth ions reduces the real and imaginary parts of permeability by weakening the magnetic interaction [109]. Although the pure sample showed a minor shift associated with eddy current loss, these values remained largely unchanged. Furthermore, two peaks that corresponded to spin resonance and natural resonance were detected close to the frequency of 11 GHz. Impedance matching was also examined by this group. They stated that impedance matching in the pure sample was weak, but with increasing doping levels up to x = 0.10 and 0.15, impedance matching approached a value close to one. The group attributed the impedance matching at x = 0.10 to improved magnetic order and the effective distribution of bismuth ions.

Todkar and his colleagues reported that doping BaM with Ce-Dy ions weakens both the real and imaginary parts of the permittivity [139]. The complex permittivity stayed constant at lower frequencies, but many resonance peaks were seen at higher frequencies. The group noted that the presence of multiple resonance peaks in μ" could be effective in enhancing the microwave absorption bandwidth. BaM exhibited high ε′ at lower frequencies, but this value decreased upon doping with Ce-Dy. The group attributed this decrease to the increase in grain size due to doping. As the grain size increases, the grain boundaries decrease, reducing the probability of electron hopping.

According to Zarrar Khan and associates, the degree of doping in $Ba_{0.5}Sr_{0.5}Fe_{12-1.1x}Zr_xY_{0.1x}O_{19}$ raises the permittivity [135]. This increase is explained by the fact that Zr^{4+} (3.25) and Y^{3+} (3.8) ions are more polarizable than Fe^{3+} (3.28). The team ascribed the several peaks in the imagined part of the permittivity to flaws and contaminants in the substance. Defects and impurities can disrupt charge balance within the structure and induce local polarization. Spin rotation and domain wall movement dictate the permeability behavior in hexaferrites. As grain size increases, domain wall movement is facilitated. With increased doping, the grain size grows, improving domain wall resonance and thereby increasing the reflection loss. Furthermore, the increase in permeability and M_s strengthens the magnetic moments. Consequently, the μ′ value decreases with increasing frequency due to the limited electron spin speed. This behavior results in optimal impedance matching.

The group also indicated that high H_a could reduce microwave absorption. In high H_a, the magnetic moments align in a specific direction in response to the electromagnetic field. However, when the H_a is lower, the magnetic moments become freer and can select different orientations. In this case, each moment can absorb different frequencies, thus increasing reflection loss.

Fig. 15 presents the reflection loss as a function of frequency and various thicknesses for SrM [194]. It is immediately clear that with changes in thickness, both the absorption frequency and the bandwidth of absorption vary. This group was able to attain a reflection loss of -17.44 dB and an effective absorption bandwidth of 2.42 GHz with a thickness of 2 mm after tweaking the conditions. It was reported that the inhomogeneity at the composite junction leads to surface polarization. Additionally, when the magnetic phase concentration exceeds a certain threshold value, the real permeability decreases. However, before this threshold, the value remains constant. The internal and external demagnetization factors dominate before and after the threshold value, respectively. Before the threshold, due to the lack of magnetic network continuity throughout the composite, the magnetic properties are related to individual magnetic particles, which corresponds to the internal demagnetization factor. In this case, the shape and structure of the individual particles affect the demagnetization factor and Ha. After the threshold value, the external demagnetization factor becomes dominant, depending on the shape and structure of the magnetic clusters. In this scenario, a magnetic flux is established throughout the composite. In this study, by increasing the concentration of the magnetic phase in the composite, the real permeability decreased due to the suppression of the internal demagnetization factor.

In 2019, a research group succeeded in achieving an absorption bandwidth spanning the entire X and Ku bands by preparing a composite consisting of 45% doped SrM, 10% copper, and 45% pure BaM [133]. They also reported that the presence of copper plays a significant role in tuning the matching frequency, leading to a broader absorption bandwidth and higher reflection loss. The group indicated that the purpose of combining pure and doped hexaferrites was to shift the resonance frequency to lower values. This observation aligns with the relationship between resonance frequency and H_a.

In another study, a composite was prepared using BaM, carbon nanotubes, and dopants such as Co, Al, and Ti [195]. The reflection loss of various compositions of the composite at different thicknesses shows that introducing carbon nanotubes forms a conductive network throughout the material, which leads to enhanced dielectric loss. In contrast, the pure BaM sample demonstrates only negligible absorption. However, with the addition of dopants and carbon nanotubes, an increase in reflection loss and absorption bandwidth can be observed. This group successfully tuned the resonance frequency within the desired range by incorporating Co, Al, and Ti dopants. The addition of carbon black and activated carbon to BaM also enhances absorption. These materials increase dipole polarization within the composite [19, 196].

A research group investigated the effects of yttrium doping in SrM on microwave absorption properties [192]. The group discovered that both the real and imaginary parts of permittivity decreased as the doping level increased because the ionic polarizability of Y (3.81 $Å^3$) is lower than that of Sr (4.24 $Å^3$), resulting in a reduction of complex permittivity. As the doping level increases, Y^{3+} ions replace Sr^{2+} ions, and some Fe^{3+} ions are converted to Fe^{2+} ions to maintain charge neutrality in the structure. As previously mentioned, electron hopping between Fe^{3+} and Fe^{2+} ions occurs, which causes energy loss.

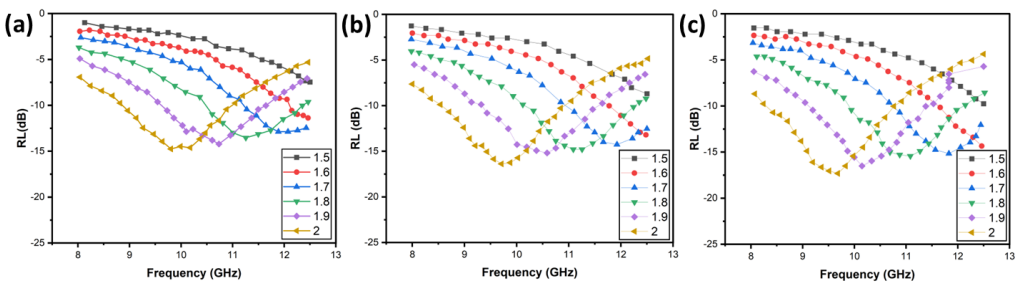

Fig. 15. a–c) Reflection loss diagram of SrM versus frequency and different thicknesses (schematic based on Ref. [194]).

The group also observed that increasing the doping level caused the resonance peaks in permeability to shift to lower frequencies. This shift was attributed to the change in anisotropy direction from the c-axis to the a-b basal plane. Moreover, permeability values increased with higher doping levels, indicating an enhancement in the effective magnetic moment of the material.

The complex permittivity of a dielectric largely depends on the ionic polarization within its structure [178]. Another group noted that a reduction in H_a enhances microwave absorption [197]. It was also demonstrated that doping BaM and converting Fe^{3+} ions to Fe^{2+} resulted in an effective absorption bandwidth with minimal thickness. The conversion of Fe^{3+} to Fe^{2+} ions within the structure creates a wide range of magnetic moments capable of absorbing a diverse set of resonance frequencies. Consequently, the absorption bandwidth increases.

H_{eff} of a nanoparticle is defined as follows [198]:

$$H_{eff} = H_d + H_a + H_{int} \quad (29)$$

For spherical nanoparticles, the H_r relationship is as follows [198]:

$$H_r = \frac{\omega}{\gamma} - H_{eff} = \frac{\omega}{\gamma} + \frac{M_s}{3} - (H_a + H_{int}) \quad (30)$$

where $H_{int} = 2m/r^3$ (r inter-particle distance and m magnetic moments) and $\omega = 2\pi f$ is the Larmor precession frequency. According to the above relationship, the distance between particles and the magnetic moment is effective in the displacement of H_r.

As mentioned, the resonant frequency of the ferromagnet in hexaferrites can be shifted by doping. Fig. 16a, b show the resonant frequency for $SrFe_{12}O_{19}$ and $SrFe_{12-x}(MgTi)_{x/2}O_{19}$ [199]. It is quite clear from Fig. 16b that the resonant frequency of the ferromagnet shifts with the changing in the amount of doping. In pure SrM, only one ferromagnetic resonance peak appears when an external field is applied. However, with doping, two resonance peaks appear. The reason for the appearance of twins is due to the large H_a in hexaferrites. The reduction of the crystalline magnetic field in doped ferrite is the reason for the shift of the resonance field to lower values.

ΔH of hexaferrites can be obtained using the following equation [169]:

$$\Delta H = \Delta H_a + \Delta H_p + \Delta H_i = 2\pi\Delta f/\gamma \quad (31)$$

In large values, ΔH_i can be ignored. ΔH of hexaferrites on $Sr_{0.7-x}La_xCa_{0.3}Fe_{11.85}Co_{0.15}O_{19}$ was calculated by An et al. [52]. The obtained values can be seen in Fig. 19c. The ΔH_s first increases up to the value x = 0.2 and then decreases. Depending on whether the value of $4\pi M_s$ is larger or smaller than H_a, the contribution of anisotropy and porosity in ΔH is determined. This group reported that $4\pi M_s$ is much smaller than H_a. In this case, the independent grain approximation (IGA) should be used. However, if the value of $4\pi M_s$ is larger than H_a, the dipolar narrowing theory (DN) should be used. Therefore, ΔH_a and ΔH_p, according to IGA theory it will be as follows [52]:

$$\Delta H = \Delta H_a + \Delta H_p \quad (32)$$

$$\Delta H_a = \frac{|K_1|}{M_s} \quad (33)$$

$$\Delta H_p = \frac{8}{\sqrt{3\pi}}(4\pi M_s)p \quad (34)$$

where p is the porosity. The calculated values for ΔH_a and ΔH_p are given in Fig. 19d. According to the figure, the value of ΔH_a increases up to x = 0.3 and then decreases, but the change in ΔH_p is small.

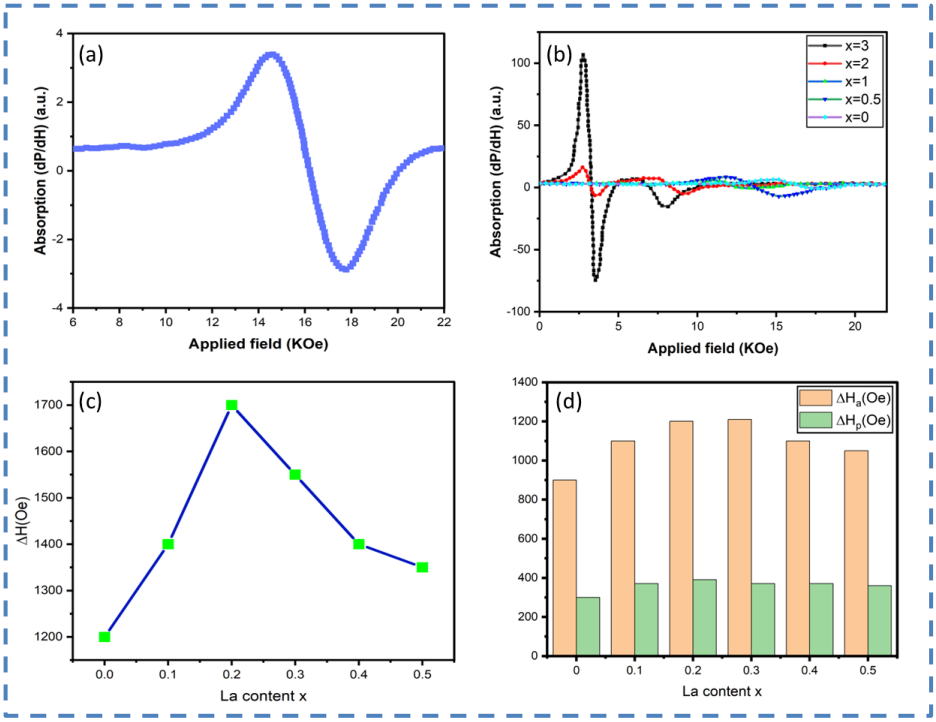

Fig. 16. Ferromagnetic resonance spectra of a) $SrFe_{12}O_{19}$, b) $SrFe_{12-x}(MgTi)_{x/2}O_{19}$ with different doping levels (schematic based on Ref. [199]), c) ΔH_a, and d) ΔH_p versus La doping amount (schematic based on Ref. [169]).

Table 5. Microwave absorption characteristics in M-type hexaferrite compounds.

Composition	Thickness (mm)	Frequency (GHz)	RL (dB)	Ref.
$BaCu_xMg_xZr_{2x}Fe_{12-4x}O_{19}$/multiwalled carbon nanotubes (MWCNTs)	2.1	8.2	-23.1	[8]
$BaFe_{12}O_{19}$/polyaniline (PANI)	0.9	33.25	-30.5	[174]
$BaFe_{12}O_{19}$/EG/carbon nanotubes (CNTs)	1	2–18	-45.8	[21]
Graphene/$CuFe_{10}Al_2O_{19}$/PANI	2.5	8.2–12.4	-63.6	[175]
$BaFe_{12-3x}(Mg_{1.5}Ti_{1.5})_xO_{19}$	2.2	13.0–17.0	-49.69	[72]
BaM/calcium copper titanate	3	15.7–17.4	-27.9	[7]
$BaFe_{12-3x}(GdAlCo)_xO_{19}$	2.07	9.73–15.27	-48.13	[143]
MWCNTs/$BaFe_{12}O_{19}$	2	≈12.00–14.56	-43.99	[20]
$Ba_{1-x}Ce_xFe_{12}O_{19}$	10	16.1	-20.40	[137]
$SrFe_{12-x}Co_xO_{19}$	2	10.9	-45.2	[193]
$BaFe_{12-x}Zr_xO_{19}$	10	≈1.50–3.25	-55	[105]
$Ba_{0.3}Sr_{0.4}Pb_{0.3}Fe_{12}O_{19}$	2	≈13.5–15.7	-57.5	[35]
$BaFe_{12-2x}(Mn_{0.5}Co_{0.5}Ti)_xO_{19}$	2.3	11.0–18.0	-40.2	[190]
$BaLa_xGd_xFe_{12-2x}O_{19}$	3	10.4	-7.8	[34]
$BaMg_{0.9}Zn_{0.9}Zr_{1.8}Fe_{8.4}O_{19}$	5	12.3	-19.3	[189]
$BaFe_{12}O_{19}$ nanoplates	2.5	8.44–12.45	-36	[188]
$BaBi_xFe_{12-x}O_{19}$	2.9	11.46–12.47	-38.78	[109]

However, ΔH_p increases up to x = 0.2 and then decreases. According to Eq. 34, decreasing porosity makes the linewidth narrower [98].

Table 5 presents the reflection loss, effective absorption bandwidth, and thickness for M-type hexaferrites and their composites. Pure hexaferrites do not exhibit satisfactory absorption properties. Based on the table, it can be observed that structures such as carbon nanotubes, polymers, and doped hexaferrites are better candidates for improving microwave absorption characteristics. Additionally, the table highlights that different nanostructures of hexaferrites have a significant impact on microwave energy dissipation. Therefore, optimizing M-type hexaferrites is essential for their application in microwave absorption.

4. Parameters affecting microwave absorption and perspectives

The factors influencing reflection loss and absorption bandwidth can generally be summarized as follows:

- **Doping**: Doping in M-type hexaferrites significantly affects microwave absorption parameters. The type and concentration of dopant ions play a crucial role, depending on their polarizability.
- **Structure**: The polycrystalline nature of hexaferrites creates densely packed grain boundaries, leading to various polarization-related losses. The surface-to-volume ratio also influences reflection loss. Additionally, structural defects and impurities act as polarization centers, enhancing absorption properties.
- **Synthesis method**: Structures synthesized through different methods exhibit varying properties. Optimizing synthesis conditions can enhance reflection loss.
- **Multicomponent structures**: Creating multicomponent structures, such as nanocomposites, introduces various interfaces. In these structures, multiple reflections and scattering of incident waves can increase energy loss. Moreover, incorporating suitable dielectric components can improve impedance matching through synergy between permittivity and permeability.
- **Thickness**: Reported results indicate that thickness affects the frequency and intensity of absorption.
- **Magnetic properties**: Reflection loss and absorption bandwidth have an inverse relationship with H_a and coercivity and a direct relationship with M_s. Lower H_a leads to effective reflection loss and broader absorption bandwidths.
- **Dielectric properties**: By modifying the permittivity of M-type hexaferrites, ionic, electronic, surface, and space-charge polarizations can be enhanced.

Recommendations for improving M-type hexaferrite absorption properties:

- **Synthesis methods**: In addition to existing methods, combining synthesis techniques, improving current methods, and optimizing conditions could yield better results.
- **Novel composite materials**: Beyond the materials already used with hexaferrites, new materials such as MXenes, metal-organic frameworks (MOFs), carbon-based structures, and polymeric frameworks could be incorporated to enhance dielectric loss in M-type hexaferrites.
- **Stability in extreme conditions**: Absorbers should be designed to maintain their microwave absorption properties under critical temperature and pressure conditions, making this an interesting area for future research.
- **Minimal thickness**: Developing composites using structures like 2D materials, which offer high surface-to-volume ratios, can achieve high absorption rates while minimizing thickness by integrating M-type hexaferrites.

- **Lightweight absorbers**: Research should focus on making absorbers lightweight by combining hexaferrites with porous structures.
- **Flexibility and stability**: Flexible and durable absorbers should be developed to ensure their suitability for various industrial applications.
- **Resistance to different weather conditions**: Investigating hydrophobic properties could lead to absorbers that retain their stability under different weather conditions.

These considerations and recommendations provide a roadmap for improving M-type hexaferrite absorbers and tailoring them for diverse applications.

5. Conclusions

In this review, the structural properties and synthesis methods of M-type hexaferrites were discussed. Based on the studies conducted, it was found that the synthesis of these materials requires high temperatures. However, the sintering temperature can be reduced by modifying parameters such as the atmospheric conditions. Additionally, varying precursor types can result in diverse nanostructures. Among the synthesis methods, the solid-state reaction and sol-gel methods were the most commonly used for preparing hexaferrites. According to the investigations, researchers primarily focused on doping these materials to enhance microwave absorption efficiency. However, achieving greater energy dissipation requires combining hexaferrites with other materials.

The magnetic properties of M-type hexaferrites were attributed to the magnetic behavior arising from Fe^{3+} ions within the structure. These Fe^{3+} ions, through super-exchange interactions, induce magnetic behavior in hexaferrites. Analysis of reflection loss graphs indicated that increasing M_s and reducing H_a significantly improve absorption properties. Additionally, in these materials, energy dissipation mechanisms such as space-charge polarization loss, ferromagnetic resonance, eddy current loss, and domain wall motion loss play critical roles in enhancing microwave energy dissipation. The fabrication of composites containing hexaferrites can further improve the reflection loss and absorption bandwidth of these materials, making them more effective for microwave absorption applications.

CRediT authorship contribution statement

Seyed Salman Seyed Afghahi: Writing – review & editing, Supervision.
Reza Torkamani: Writing – original draft, Writing – review & editing.
Pouria Dehghani: Writing – review & editing.

Data availability

The data underlying this article will be shared on reasonable request to the corresponding author.

Declaration of competing interest

The authors declare no competing interests.

Funding and acknowledgment

This research received no external funding. The authors have no acknowledgments to declare.

References

[1] R. Peymanfar, F. Fazlalizadeh, Microwave absorption performance of ZnAl2O4, Chem. Eng. J. 402 (2020) 126089. https://doi.org/10.1016/j.cej.2020.126089.
[2] T.D. Thanh, N. Tran, N.T.V. Chinh, T.T.H. Giang, N.Q. Tuan, Development of high-efficiency tri-layer microwave absorbing materials based on SrMeFe11O19 hexaferrite, J. Alloys Compd. 970 (2024) 172421. https://doi.org/10.1016/j.jallcom.2023.172421.
[3] N. Shao, J. Li, S. Che, J. Zheng, L. Qiao, et al., L and S band microwave absorption properties of Z-type hexaferrite Ba3Co2Fe24O41 synthesized at low temperature, J. Alloys Compd. 968 (2023) 171926. https://doi.org/10.1016/j.jallcom.2023.171926.
[4] S.I. Popoola, N. Faruk, A.A. Atayero, M.A. Oshin, O.W. Bello, E. Mutafungwa, Radio access technologies for sustainable deployment of 5G networks in emerging markets, Int. J. Appl. Eng. Res. 12 (2017) 14154–14172.
[5] W. Aiqiong, J. Li, M. Chen, X. Zhao, A review of graphene-based broad bandwidth microwave absorbing textile-based composites in the low-frequency range, J. Ind. Text. 52 (2022). https://doi.org/10.1177/15280837221133113.
[6] S. Ghosh, P. Rangaiah, M. Aboulsaad, S. Slimani, J. Cedervall, et al., Biphasic lithium iron oxide nanocomposites for enhancement in electromagnetic interference shielding properties, J. Alloys Compd. 1010 (2025) 177017. https://doi.org/10.1016/j.jallcom.2024.177017.
[7] J. Mohammed, T.T.T. Carol, H.Y. Hafeez, D. Basandrai, G.R. Bhadu, et al., Electromagnetic interference (EMI) shielding, microwave absorption, and optical sensing properties of BaM/CCTO composites in Ku-band, Results Phys. 13 (2019) 102307. https://doi.org/10.1016/j.rinp.2019.102307.
[8] H. Nikmanesh, M. Moradi, G.H. Bordbar, R.S. Alam, Synthesis of multi-walled carbon nanotube/doped barium hexaferrite nanocomposites: An investigation of structural, magnetic and microwave absorption properties, Ceram. Int. 42 (2016) 14342–14349. https://doi.org/10.1016/j.ceramint.2016.05.089.
[9] M. Zahid, S. Siddique, R. Anum, M.F. Shakir, Y. Nawab, Z.A. Rehan, M-type barium hexaferrite-based nanocomposites for EMI shielding application: a review, J. Supercond. Nov. Magn. 34 (2021) 1019–1045. https://doi.org/10.1007/s10948-021-05859-1.
[10] S.A. Khan, I. Ali, A. Hussain, H.M.A. Javed, V.A. Turchenko, et al., Synthesis and characterization of composites with Y-hexaferrites for electromagnetic interference shielding applications, Magnetochemistry. 8 (2022) 186. https://doi.org/10.3390/magnetochemistry8120186.
[11] Y. Han, M. He, J. Hu, P. Liu, Z. Liu, et al., Hierarchical design of FeCo-based microchains for enhanced microwave absorption in C band, Nano Res. 16 (2023) 1773–1778. https://doi.org/10.1007/s12274-022-5111-y.
[12] N. Tran, R. Yang, W.H. Jeong, D.H. Manh, T. Phan, B.W. Lee, Enhanced microwave absorption features of Ba3Co2Fe24O41 hexaferrite by high lanthanium doping concentration, J. Am. Ceram. Soc. 105 (2022) 4122–4134. https://doi.org/10.1111/jace.18378.
[13] X. Ren, X. Pu, H. Yin, Y. Tang, H. Yuan, H. Fan, Fabrication of hierarchical PANI@W-type barium hexaferrite composites for highly efficient microwave absorption, Ceram. Int. 47 (2021) 12122–12129. https://doi.org/10.1016/j.ceramint.2021.01.057.
[14] T.D. Thanh, N. Tran, N.T.V. Chinh, N.T.N. Anh, N. Tuan, Excellent microwave absorption performances of cobalt-doped SrFe12O19 hexaferrite with varying incident angles, J. Alloys Compd. 952 (2023) 170060. https://doi.org/10.1016/j.jallcom.2023.170060.
[15] S. Goel, A. Garg, R.K. Gupta, A. Dubey, N.E. Prasad, S. Tyagi, Effect of neodymium doping on microwave absorption property of barium hexaferrite in X-band, Mater. Res. Express. 7 (2020) 16109. https://doi.org/10.1088/2053-1591/ab6544.
[16] R.C. Pullar, P. Galizia, A.C.C. Migliano, J.S. Amaral, C. Galassi, F.E. Carvalho, The ferromagnetic resonance (FMR) of SrZ

hexaferrite (Sr3Co2Fe24O41), and the tuning of FMR with an external magnetic field, Ceram. Int. 49 (2023) 24407–24413. https://doi.org/10.1016/j.ceramint.2022.11.264.
[17] S. Pakniyakan, B. Aslibeiki, Electromagnetic waves absorbing performance of cypress cone derived activated carbon decorated by magnetite nanoparticles, Diam. Relat. Mater. 147 (2024) 111324. https://doi.org/10.1016/j.diamond.2024.111324.
[18] M. Mahmoodi, B. Aslibeiki, R. Peymanfar, H. Naghshara, R.K. Rajagopal, et al., Electromagnetic wave absorption performance of Fe3O4/activated carbon-natural resin nanocomposite, New Carbon Mater. 39 (2024) 1157–1177. https://doi.org/10.1016/S1872-5805(24)60888-7.
[19] S. Goel, A. Garg, H.B. Baskey, M.K. Pandey, S. Tyagi, Studies on dielectric and magnetic properties of barium hexaferrite and bio-waste derived activated carbon composites for X-band microwave absorption, J. Alloys Compd. 875 (2021) 160028. https://doi.org/10.1016/j.jallcom.2021.160028.
[20] N. Rosdi, R.S. Azis, I. Ismail, N. Mokhtar, M.M. Muhammad Zulkimi, M.S. Mustaffa, Structural, microstructural, magnetic and electromagnetic absorption properties of spiraled multiwalled carbon nanotubes/barium hexaferrite (MWCNTs/BaFe12O19) hybrid, Sci. Rep. 11 (2021) 15982. https://doi.org/10.1038/s41598-021-95332-9.
[21] T. Zhao, W. Jin, X. Ji, H. Yan, Y. Jiang, et al., Synthesis of sandwich microstructured expanded graphite/barium ferrite connected with carbon nanotube composite and its electromagnetic wave absorbing properties, J. Alloys Compd. 712 (2017) 59–68. https://doi.org/10.1016/j.jallcom.2017.04.070.
[22] M. Forushani, G. Gordani, A. Ghasemi, M. Estarki, S. Torkian, et al., Effect of multi-wall carbon nanotubes/strontium ferrite nanoparticles on the microstructure, phase, magnetic and electromagnetic behavior of carbon aerogel composites, J. Mater. Res. Technol. 23 (2023) 3424–3440. https://doi.org/10.1016/j.jmrt.2023.01.135.
[23] Y. Song, F. Yin, C. Zhang, W. Guo, L. Han, Y. Yuan, Three-dimensional ordered mesoporous carbon spheres modified with ultrafine zinc oxide nanoparticles for enhanced microwave absorption properties, Nano-micro Lett. 13 (2021) 1–16. https://doi.org/10.1007/s40820-021-00601-x.
[24] S. Gupta, C. Chang, A.K. Anbalagan, C.-H. Lee, N.-H. Tai, Reduced graphene oxide/zinc oxide coated wearable electrically conductive cotton textile for high microwave absorption, Compos. Sci. Technol. 188 (2020) 107994. https://doi.org/10.1016/j.compscitech.2020.107994.
[25] Q. Xia, X. Wang, Z. Huang, L. Chen, C. Li, et al., The lightweight titanium dioxide/reduced graphene oxide composites prepared by hydrothermal method for microwave absorption, J. Alloys Compd. 1003 (2024) 175640. https://doi.org/10.1016/j.jallcom.2024.175640.
[26] K. Hu, H. Wang, X. Zhang, H. Huang, T. Qiu, et al., Ultralight Ti3C2Tx MXene foam with superior microwave absorption performance, Chem. Eng. J. 408 (2021) 127283. https://doi.org/10.1016/j.cej.2020.127283.
[27] C. Wen, X. Li, R. Zhang, C. Xu, W. You, et al., High-density anisotropy magnetism enhanced microwave absorption performance in Ti3C2T x MXene@ Ni microspheres, ACS Nano. 16 (2021) 1150–1159. https://doi.org/10.1021/acsnano.1c08957.
[28] X. Zhou, J. Wen, Z. Wang, X. Ma, H. Wu, Broadband high-performance microwave absorption of the single-layer Ti3C2Tx MXene, J. Mater. Sci. Technol. 115 (2022) 148–155. https://doi.org/10.1016/j.jmst.2021.11.029.
[29] P. Liu, S. Gao, Y. Wang, F. Zhou, Y. Huang, J. Luo, Metal-organic polymer coordination materials derived Co/N-doped porous carbon composites for frequency-selective microwave absorption, Compos. B: Eng. 202 (2020) 108406. https://doi.org/10.1016/j.compositesb.2020.108406.
[30] P. Miao, N. Qu, W. Chen, T. Wang, W. Zhao, J. Kong, A two-dimensional semiconductive Cu-S metal-organic framework for broadband microwave absorption, Chem. Eng. J. 454 (2023) 140445. https://doi.org/10.1016/j.cej.2022.140445.
[31] X. Zhou, J. Wang, L. Zhou, Y. Wang, D. Yao, Structure, magnetic and microwave absorption properties of NiZnMn ferrite ceramics, J. Magn. Magn. Mater. 534 (2021) 168043. https://doi.org/10.1016/j.jmmm.2021.168043.
[32] 최성준, Microwave absorption properties of Zn-substituted W-type hexaferrites and carbonyl iron for 5G communication, Thesis, 서울대학교 대학원. (2021).
[33] A. Houbi, Z.A. Aldashevich, Y. Atassi, Z.B. Telmanovna, M. Saule, K. Kubanych, Microwave absorbing properties of ferrites and their composites: A review, J. Magn. Magn. Mater. 529 (2021) 167839. https://doi.org/10.1016/j.jmmm.2021.167839.
[34] F. Abdollahi, M. Yousefi, M. Hekmati, A. Khajehnezhad, S.S. Seyyed Afghahi, Magnetic and microwave absorption properties of barium hexaferrite doped with La3+ and Gd3+, J. Nanostructures. 9 (2019) 579–586. https://doi.org/10.22052/JNS.2019.03.019.
[35] A. Baykal, İ.S. Ünver, U. Topal, H. Sözeri, Pb substituted Ba, Sr-hexaferrite nanoparticles as high quality microwave absorbers, Ceram. Int. 43 (2017) 14023–14030. https://doi.org/10.1016/j.ceramint.2017.07.134.
[36] A.J. Lere-Adams, M. Ahmadzadeh, N. Smith-Gray, D. Bollinger, S. Boroughs, J.S. McCloy, In situ crystallization and magnetic measurement of hexaferrite glass-ceramics, AIP Adv. 11 (2021). https://doi.org/10.1063/9.0000063.
[37] K.-P. Jeong, J.-G. Kim, S.-W. Yang, J.-H. Yun, J.-H. Choi, Study on magnetic properties of the U-type ferrite according to substituted elements, Arch. Metall. Mater. 64 (2019) 501–505. https://doi.org/10.24425/amm.2019.127567.
[38] A. Majeed, M.A. Khan, R. Ahmad, M.Y. Lodhi, I. Ahmad, Influence of Cr and Zn substitution on structural, magnetic and dielectric properties of Sr2-xZnxNi2Fe28-yCryO46 X-type hexagonal ferrite, Solid State Sci. 100 (2020) 106090. https://doi.org/10.1016/j.solidstatesciences.2019.106090.
[39] M.K. Dmour, E.S. Al-Hwaitat, Y. Maswadeh, I. Bsoul, S.H. Mahmood, Preparation and characterization of rare earth-zinc substituted X-type hexaferrites, J. Alloys Compd. 836 (2020) 155396. https://doi.org/10.1016/j.jallcom.2020.155396.
[40] A. Dhingra, O.P. Thakur, R. Pandey, Enhanced magnetic properties of single domain Al-substituted strontium hexaferrite (SrFe12−xAlxO19) synthesized via hydrothermal method for permanent magnets, J. Alloys Compd. (2024) 175132. https://doi.org/10.1016/j.jallcom.2024.175132.
[41] T. Reimann, T. Schmidt, J. Töpfer, Phase stability and magnetic properties of SrFe18O27 W-type hexagonal ferrite, J. Am. Ceram. Soc. 103 (2020) 324–334. https://doi.org/10.1111/jace.16726.
[42] L.A. Trusov, A.E. Sleptsova, J. Duan, E. Gorbachev, E. Kozlyakova, et al., Glass-ceramic synthesis of cr-substituted strontium hexaferrite nanoparticles with enhanced coercivity, Nanomaterials. 11 (2021) 924. https://doi.org/10.3390/nano11040924.
[43] R.V. Minin, V.I. Itin, V.A. Zhuravlev, Effect of mechanical activation and ferritization on the phase composition of W-type hexaferrites obtained by the method of self-propagating high-temperature synthesis, J. Phys. Conf. Ser. 1459 (2020) 12016. https://doi.org/10.1088/1742-6596/1459/1/012016.
[44] Y.D. Choudhari, K.G. Rewatkar, Influence of Bi3+ ions substitution on structural, magnetic, and electrical properties of lead hexaferrite, J. Magn. Magn. Mater. 551 (2022) 169162. https://doi.org/10.1016/j.jmmm.2022.169162.
[45] S. Prathap, W. Madhuri, S.S. Meena, Multiferroic properties and Mössbauer Study of M-type hexaferrite PbFe12O19 synthesized by the high energy ball milling, Mater. Charact. 177 (2021) 111168. https://doi.org/10.1016/j.matchar.2021.111168.
[46] K. Singha, R. Jasrotia, L.W.Y. Liu, J. Prakash, A. Verma, et al., A review of Z-type hexaferrite based magnetic nanomaterials: structure, synthesis, properties, and potential applications, Prog. Solid State Chem. 70 (2023) 100404. https://doi.org/10.1016/j.progsolidstchem.2023.100404.

[47] G. Khazaradze, D. Daraselia, D. Japaridze, A. Shengelaya, Magnetoelectric coupling in Y-type hexaferrite studied by a novel magnetic resonance technique, Magn. Reson. Solids. Electron. J. 21 (2019) 19307.
[48] Y. Shao, F. Huang, J. Zhang, S. Yan, S. Xiao, et al., Magnetoelectric coupling triggered by noncollinear magnetic structure in M-type hexaferrite, Adv. Quantum Technol. 4 (2021) 2000096. https://doi.org/10.1002/qute.202000096.
[49] M.M. Arman, Structural, morphological and magnetic properties of hexaferrite BaCo2Fe16O27 nanoparticles and their efficient lead removal from water, Appl. Phys. A. 128 (2022) 1103. https://doi.org/10.1007/s00339-022-06244-y.
[50] T. Gupta, C.C. Chauhan, S.S. Meena, A.A. Gor, R. Meena, et al., Influence of Sm and Cd co-substitutions on physical, magnetic, Mössbauer, electric, and dielectric properties of Co2X hexagonal ferrites in presence of a hematite phase, Ceram. Int. 48 (2022) 36802–36813. https://doi.org/10.1016/j.ceramint.2022.08.244.
[51] V. Dixit, S.-G. Kim, J. Park, Y. Hong, Effect of ionic substitutions on the magnetic properties of strontium hexaferrite: a first principles study, AIP Adv. 7 (2017) 115209. https://doi.org/10.1063/1.4995309.
[52] G.-H. An, T.-Y. Hwang, J. Kim, J. Kim, N. Kang, et al., Barium hexaferrite nanoparticles with high magnetic properties by salt-assisted ultrasonic spray pyrolysis, J. Alloys Compd. 583 (2014) 145–150. https://doi.org/10.1016/j.jallcom.2013.08.105.
[53] Z. Irshad, I. Bibi, A. Ghafoor, F. Majid, S. Kamal, et al., Ni doped SrFe12O19 nanoparticles synthesized via micro-emulsion route and photocatalytic activity evaluation for the degradation of crystal violet under visible light irradiation, Results Phys. 42 (2022) 106006. https://doi.org/10.1016/j.rinp.2022.106006.
[54] S.R. Ejaz, M.A. Khan, S. Gulbadan, M.N. Akhtar, M. Ahmad, et al., Structural, spectral, dielectric and magnetic properties of Co–Cr-substituted hexagonal ferrites with X-type structure, J. Korean Ceram. Soc. 59 (2022) 453–464. https://doi.org/10.1007/s43207-022-00203-2.
[55] D.V. Wagner, V.A. Zhuravlev, K.V. Kareva, R.V. Minin, K.I. Baskakova, et al., Ba2Co2-xZnxFe12O22 Hexaferrites produced by the method of self-propagating high-temperature synthesis: Structure, properties, application, J. Alloys Compd. 977 (2024) 173437. https://doi.org/10.1016/j.jallcom.2024.173437.
[56] A.R. Kagdi, N.P. Solanki, F.E. Carvalho, S.S. Meena, P. Bhatt, et al., Influence of Mg substitution on structural, magnetic and dielectric properties of X-type bariumzinc hexaferrites Ba2Zn2-xMgxFe28O46, J. Alloys Compd. 741 (2018) 377–391. https://doi.org/10.1016/j.jallcom.2018.01.092.
[57] S. Kaur, A. Sharma, N. Thakur, Basic Physics and Chemistry of Ferrites, Engineered Ferrites and Their Applications. Materials Horizons: From Nature to Nanomaterials, Springer, Singapore. (2023) 1–15. https://doi.org/10.1007/978-981-99-2583-4_1.
[58] H.B. Cao, Z.Y. Zhao, M. Lee, E.S. Choi, M.A. McGuire, et al., High pressure floating zone growth and structural properties of ferrimagnetic quantum paraelectric BaFe12O19, APL Mater. 3 (2015) 062512. https://doi.org/10.1063/1.4922934.
[59] M. Chandel, V.P. Singh, R. Jasrotia, K. Singha, R. Kumar, A review on structural, electrical and magnetic properties of Y-type hexaferrites synthesized by different techniques for antenna applications and microwave absorbing characteristic materials, AIMS Mater. Sci. 7 (2020) 244–268. https://doi.org/10.3934/matersci.2020.3.244.
[60] A. Gholizadeh, V. Banihashemi, Effects of Ca−Gd co-substitution on the structural, magnetic, and dielectric properties of M-type strontium hexaferrite, J. Am. Ceram. Soc. 106 (2023) 5351–5363. https://doi.org/10.1111/jace.19191.
[61] J. Chen, Y. Liu, Y. Wang, Q. Yin, Q. Liu, et al., Magnetic and microwave properties of polycrystalline U-type hexaferrite Ba4Zn2−xCoxFe36O60, J. Magn. Magn. Mater. 496 (2020) 165948. https://doi.org/10.1016/j.jmmm.2019.165948.
[62] M. Suthar, P.K. Roy, Structural, electromagnetic, and Ku-band absorption characterization of La-Mg substituted Y-type barium hexaferrite for EMI shielding application, Mater. Sci. Eng. B. 283 (2022) 115801. https://doi.org/10.1016/j.mseb.2022.115801.
[63] H.K. Ye, S.R. Shannigrahi, C.B. Soh, S.L.W. Yang, L.S. Li, et al., Development of (Zr, Mn) doped X-type hexaferrites for high frequency EMI shielding applications, J. Magn. Magn. Mater. 465 (2018) 716–726. https://doi.org/10.1016/j.jmmm.2018.06.050.
[64] D. Lisjak, D. Makovec, M. Drofenik, Formation of U-type hexaferrites, J. Mater. Res. 19 (2004) 2462–2470. https://doi.org/10.1557/JMR.2004.0317.
[65] M.I. Mørch, J.V. Ahlburg, M. Saura-Múzquiz, A.Z. Eikeland, M. Christensen, Structure and magnetic properties of W-type hexaferrites, IUCrJ. 6 (2019) 492–499. https://doi.org/10.1107/S2052252519003130.
[66] H.N. Chaudhari, R.C. Pullar, S.S. Meena, C. Singh, S. Municoy, et al., Al 3+ substituted U-type hexaferrites Ba4Co2Fe36−xAlxO60: structural, magnetic, electrical and dielectric properties, J. Mater. Chem. C. 12 (2024) 15621–15643. https://doi.org/10.1039/D4TC01659A.
[67] A.S. Muhammad, M. Irfan, M.N. Akhtar, M.A. Khan, Recent Advances in U-type hexagonal ferrites: Synthesis, Characterizations, Magnetic and Absorption Properties, Hybrid Adv. 7 (2024) 100324. https://doi.org/10.1016/j.hybadv.2024.100324.
[68] M. Soroka, J. Buršík, R. Kužel, L. Horák, J. Prokleška, et al., Epitaxial growth of thin films of X-type Sr2Co2Fe28O46 hexaferrite by chemical solution deposition, J. Eur. Ceram. Soc. 43 (2023) 6916–6924. https://doi.org/10.1016/j.jeurceramsoc.2023.07.027.
[69] F.F. Barbosa, J. de Oliveira Soares, M.O. Miranda, M.A.M. Torres, T.P. Braga, Catalysis Application of Magnetic Ferrites and Hexaferrites, Handbook of Magnetic Hybrid Nanoalloys and their Nanocomposites, Springer, Cham. (2022) 1–42. https://doi.org/10.1007/978-3-030-90948-2_48.
[70] M.U. Shafi, M.A. Khan, M. Irfan, M.N. Akhtar, A review on advances in synthesis, composition, structural and microwave properties of U-type hexaferrites nanoparticles, J. Mater. Sci. 59 (2024) 16383–16410. https://doi.org/10.1007/s10853-024-10180-y.
[71] H.M. Khan, M. Mustaqeem, Y.-F. Chen, M. Junaid, T.A. Saleh, et al., Tuning of structural and dielectric properties of X type hexaferrite through Co and Zn variation, J. Alloys Compd. 909 (2022) 164529. https://doi.org/10.1016/j.jallcom.2022.164529.
[72] M.H. Shams, S.M.A. Salehi, A. Ghasemi, Electromagnetic wave absorption characteristics of Mg–Ti substituted Ba-hexaferrite, Mater. Lett. 62 (2008) 1731–1733. https://doi.org/10.1016/j.matlet.2007.09.073.
[73] A. Kalariya, T. Gupta, C.C. Chauhan, R.B. Jotania, Exploring structural, magnetic and dielectric properties of Ba1−xCoxFe12O19 hexaferrites, J. Mater. Sci. Mater. Electron. 35 (2024) 696. https://doi.org/10.1007/s10854-024-12441-7.
[74] M. Yousefi, S.S.S. Afghahi, M.M. Amini, M.B. Torbati, An investigation of structural and magnetic properties of Ce–Nd doped strontium hexaferrite nanoparticles as a microwave absorbent, Mater. Chem. Phys. 235 (2019) 121722. https://doi.org/10.1016/j.matchemphys.2019.121722.
[75] X. Zhang, Y. Zhang, Z. Yue, J. Zhang, Influences of sintering atmosphere on the magnetic and electrical properties of barium hexaferrites, AIP Adv. 9 (2019) 085129. https://doi.org/10.1063/1.5111422.
[76] C.G. Knudsen, M.I. Mørch, M. Christensen, Texture formation in W-type hexaferrite by cold compaction of non-magnetic interacting anisotropic shaped precursor crystallites, Dalt. Trans. 52 (2023) 281–289. https://doi.org/10.1039/D2DT02091B.
[77] P. Li, M. Yu, L. Yang, Q. Duan, Y. Wu, et al., Mutual control of electric and magnetic orders near room temperature in Al doped Y-type hexaferrite single crystals, J. Mater. 11 (2025) 100867. https://doi.org/10.1016/j.jmat.2024.03.012.

[78] S. Shen, L. Yan, Y. Chai, J. Cong, Y. Sun, Magnetic field reversal of electric polarization and magnetoelectric phase diagram of the hexaferrite Ba1.3Sr0.7Co0.9Zn1.1Fe10.8Al1.2O22, Appl. Phys. Lett. 104 (2014) 032905. https://doi.org/10.1063/1.4862690.
[79] K. Zhai, D. Shang, Y. Chai, G. Li, J. Cai, et al., Room-temperature nonvolatile memory based on a single-phase multiferroic hexaferrite, Adv. Funct. Mater. 28 (2018) 1705771. https://doi.org/10.1002/adfm.201705771.
[80] R.B. Jotania, H.S. Virk, Y-type Hexaferrites: structural, dielectric and magnetic properties, Solid State Phenom. 189 (2012) 209–232. https://doi.org/10.4028/www.scientific.net/SSP.189.209.
[81] M. Komabuchi, D. Urushihara, T. Asaka, K. Fukuda, T. Ohhara, et al., Crystal Structure and Cation Distribution of the X-type Hexaferrite Sr2Co2Fe28O46, J. Phys. Soc. Jpn. 89 (2020) 34601. https://doi.org/10.7566/JPSJ.89.034601.
[82] I. Mohammed, J. Mohammed, A.K. Srivastava, Recent progress in hexagonal ferrites based composites for microwave absorption, Cryst. Res. Technol. 58 (2023) 2200200. https://doi.org/10.1002/crat.202200200.
[83] S.H. Mahmood, M.D. Zaqsaw, O.E. Mohsen, A. Awadallah, I. Bsoul, et al., Modification of the magnetic properties of Co2Y hexaferrites by divalent and trivalent metal substitutions, Solid State Phenom. 241 (2016) 93–125. https://doi.org/10.4028/www.scientific.net/SSP.241.93.
[84] R. Jasrotia, J. Prakash, R. Verma, P. Thakur, A. Kandwal, et al., Synthesis, characterization, and applications of doped barium hexaferrites: A review, Phys. B: Condens. Matter. 667 (2023) 415202. https://doi.org/10.1016/j.physb.2023.415202.
[85] B. Abasht, S.M. Mirkazemi, A. Beitollahi, Solution combustion synthesis of Ca hexaferrite using glycine fuel, J. Alloys Compd. 708 (2017) 337–343. https://doi.org/10.1016/j.jallcom.2017.03.036.
[86] M.L. Rahman, S. Rahman, B. Biswas, M.F. Ahmed, M. Rahman, N. Sharmin, Investigation of structural, morphological and magnetic properties of nanostructured strontium hexaferrite through co-precipitation technique: Impacts of annealing temperature and Fe/Sr ratio, Heliyon. 9 (2023) e14532. https://doi.org/10.1016/j.heliyon.2023.e14532.
[87] H. Shirmahd, M. Aboutalebi, S.H. Seyedein, M. Adeli, Synthesis of strontium hexaferrite (SrFe12O19) by self-propagating high-temperature synthesis (SHS) method and investigation of the effect of milling on morphology and magnetic properties, Ceram. Int. 50 (2024) 38542–38549. https://doi.org/10.1016/j.ceramint.2024.07.222.
[88] S. Mahmood, I. Bsoul, Tuning the magnetic properties of M-type hexaferrites, Magnetic Oxides and Composites, Materials Research Forum. (2017). https://doi.org/10.21741/9781945291692-2.
[89] R. Jasrotia, J. Prakash, N. Thakur, K. Raj, A. Kandwal, P. Sharma, Advancements in doping strategies for enhancing applications of M-type hexaferrites: a comprehensive review, Prog. Solid State Chem. 72 (2023) 100427. https://doi.org/10.1016/j.progsolidstchem.2023.100427.
[90] C. Qin, R. Liu, Y. Sun, J. Wu, T. Zhao, H. Gong, Phase formation and magnetic properties of M-type lanthanum substituted strontium ferrites, Ceram. Int. 49 (2023) 30924–30936. https://doi.org/10.1016/j.ceramint.2023.07.171.
[91] R.C. Pullar, Hexagonal ferrites: a review of the synthesis, properties and applications of hexaferrite ceramics, Prog. Mater. Sci. 57 (2012) 1191–1334. https://doi.org/10.1016/j.pmatsci.2012.04.001.
[92] J. Le Breton, V. Nachbaur, O. Fitchorova, Hexaferrite Permanent Magnets and Applications, Mod. Ferrites Emerg. Technol. Appl. 2 (2022) 91–101. https://doi.org/10.1002/9781394156146.ch4.
[93] B. Grindi, A. Benali, C. Magén, G. Viau, M-SrFe12O19 and ferrihydrite-like ultrathin nanoplatelets as building blocks for permanent magnets: HAADF-STEM study and magnetic properties, J. Solid State Chem. 264 (2018) 124–133. https://doi.org/10.1016/j.jssc.2018.05.015.
[94] H. Ikeno, Density functional calculations of the Mössbauer parameters in hexagonal ferrite SrFe12O19, Phys. B: Condens. Matter. 532 (2018) 20–23. https://doi.org/10.1016/j.physb.2017.01.026.
[95] J. Hlosta, K. Hrabovská, J. Rozbroj, J. Nečas, D. Žurovec, et al., Influence of calcination temperature and particle size distribution on the physical properties of SrFe12O19 and BaFe12O19 hexaferrite powders, Sci. Rep. 14 (2024) 17564. https://doi.org/10.1038/s41598-024-67994-8.
[96] S.V. Trukhanov, A.V. Trukhanov, V.G. Kostishyn, L.V. Panina, A.V. Trukhanov, et al., Investigation into the structural features and microwave absorption of doped barium hexaferrites, Dalt. Trans. 46 (2017) 9010–9021. https://doi.org/10.1039/C7DT01708A.
[97] C. de Julian Fernandez, C. Sangregorio, J. de la Figuera, B. Belec, D. Makovec, A. Quesada, Progress and prospects of hard hexaferrites for permanent magnet applications, J. Phys. D. Appl. Phys. 54 (2021) 153001. https://doi.org/10.1088/1361-6463/abd272.
[98] Q. Liu, C. Wu, Y. Wang, L. Zhou, J. Li, et al., Textured M-type barium hexaferrite Ba(ZnSn)xFe12−2xO19 with c-axis anisotropy and high squareness ratio, Ceram. Int. 45 (2019) 4535–4539. https://doi.org/10.1016/j.ceramint.2018.11.138.
[99] C. Liu, X. Kan, X. Liu, S. Feng, J. Hu, et al., Influence of the Eu substitution on the structure and magnetic properties of the Sr-hexaferrites, Ceram. Int. 46 (2020) 171–179. https://doi.org/10.1016/j.ceramint.2019.08.245.
[100] M. Zahid, H.M. Khan, M.A. Assiri, M. Imran, S.A. Buzdar, Structural, morphological, dielectric, and magnetic properties of Pb1-xCrxFe12O19 M-type hexaferrites, Mater. Sci. Eng. B. 280 (2022) 115707. https://doi.org/10.1016/j.mseb.2022.115707.
[101] C. Granados-Miralles, P. Jenuš, On the potential of hard ferrite ceramics for permanent magnet technology—a review on sintering strategies, J. Phys. D. Appl. Phys. 54 (2021) 303001. https://doi.org/10.1088/1361-6463/abfad4.
[102] N. Asiabani, G. Nabiyouni, S. Khaghani, D. Ghanbari, Green synthesis of magnetic and photo-catalyst PbFe 12O19−PbS nanocomposites by lemon extract: nano-sphere PbFe12O19 and star-like PbS, J. Mater. Sci. Mater. Electron. 28 (2017) 1101–1114. https://doi.org/10.1007/s10854-016-5635-6.
[103] C. Qin, Y. Sun, Z. Li, R. Liu, X. Jing, et al., Effect of Fe deficiency on the crystalline structure and magnetic properties of M-type strontium hexaferrite, Arab. J. Chem. (2023) 105092. https://doi.org/10.1016/j.arabjc.2023.105092.
[104] S.U. Asif, U.-R. Ghori, M. Ahsan, F. Ahmed, E.A.M. Saleh, et al., Structural and magnetic influence by mg on BaFe10Al2O19 hexaferrites prepared via ceramic route for potential magnetic applications, J. Mater. Sci. Mater. Electron. 34 (2023) 2211. https://doi.org/10.1007/s10854-023-11645-7.
[105] M.A. Darwish, H.F. Abosheiasha, A.T. Morchenko, V.G. Kostishyn, V.A. Turchenko, et al., Impact of the Zr-substitution on phase composition, structure, magnetic, and microwave properties of the BaM hexaferrite, Ceram. Int. 47 (2021) 16752–16761. https://doi.org/10.1016/j.ceramint.2021.02.247.
[106] M. Ijaz, H. Ullah, B.A. Al-Asbahi, M.U. Khan, Z. Abbas, S.U. Asif, Co-precipitation method followed by ultrafast sonochemical synthesis of aluminium doped M type BaFe11.4-xAlxCo0.6O19 hexaferrites for various applications, J. Magn. Magn. Mater. 589 (2024) 171559. https://doi.org/10.1016/j.jmmm.2023.171559.
[107] S. Susilawati, A. Doyan, M. Taufik, W. Wahyudi, The structure of barium M-hexaferrite (BaFe12-2xCoxNixO19) powders using co-precipitation methods, AIP Conf. Proc. 2251 (2020) 040028. https://doi.org/10.1063/5.0015750.
[108] T. Jayakumar, S. Arumugam, Structural confirmation and elucidation of spectral, optical and magnetic properties of cerium doped lead hexaferrite, Mater. Lett. 277 (2020) 128309. https://doi.org/10.1016/j.matlet.2020.128309.
[109] R. Duglet, A. Chauhan, D. Sharma, A. Thakur, M. Singh, Investigation on microwave absorption properties of bismuth ions doped barium hexaferrites, J. Mater. Sci. Mater. Electron. 35 (2024) 654. https://doi.org/10.1007/s10854-024-12418-6.

[110] T.H. Mubarak, O.A. Mahmood, Z.J. Hamakhan, Structural, magnetic and electrical properties of Ba2Mg2Fe28O46 (Mg2X) hexaferrites, Int. J. Appl. Eng. Res. 13 (2018) 6369.
[111] A. Bhaduri, S. Singh, K.B. Thapa, B.C. Yadav, Visible light-induced, highly responsive, below lower explosive limit (LEL) LPG sensor based on hydrothermally synthesized barium hexaferrite nanorods, Sens. Actuators B: Chem. 348 (2021) 130714. https://doi.org/10.1016/j.snb.2021.130714.
[112] G.D. Soria, P. Jenus, J.F. Marco, A. Mandziak, M. Sanchez-Arenillas, et al., Strontium hexaferrite platelets: a comprehensive soft X-ray absorption and Mössbauer spectroscopy study, Sci. Rep. 9 (2019) 11777. https://doi.org/10.1038/s41598-019-48010-w.
[113] S. Tyagi, R.C. Agarwala, V. Agarwala, Reaction kinetic studies of strontium hexaferrite nanoparticles synthesized by co-precipitation method, Trans. Indian Inst. Met. 63 (2010) 15–19. https://doi.org/10.1007/s12666-010-0003-3.
[114] H. Li, X. Yi, Y. Wu, X. Wei, D. Deng, et al., Molten salt synthesis, formation mechanism and greatly enhanced magnetic properties of randomly oriented BaM ferrite, J. Alloys Compd. 827 (2020) 154083. https://doi.org/10.1016/j.jallcom.2020.154083.
[115] M. Kim, K. Lee, C. Bae, J. Kim, Magnetic and morphological properties of Ca substituted M-type hexaferrite powders synthesized by the molten salt method, AIP Adv. 11 (2021) 055310. https://doi.org/10.1063/5.0041533.
[116] S. Akhtar, S. Saba, S. Rehman, A. Hassan, N. Samad, et al., Microemulsion-based synthesis of strontium hexaferrite cobalt iron oxide nanoparticles and their biocompatibility in albino mice, J. Exp. Nanosci. 13 (2018) 199–211. https://doi.org/10.1080/17458080.2018.1475759.
[117] F. Bibi, S. Iqbal, H. Sabeeh, T. Saleem, B. Ahmad, et al., Evaluation of structural, dielectric, magnetic and photocatalytic properties of Nd and Cu co-doped barium hexaferrite, Ceram. Int. 47 (2021) 30911–30921. https://doi.org/10.1016/j.ceramint.2021.07.274.
[118] S.S. Seyyed Afghahi, M. Jafarian, Synthesis and evaluation of physical and magnetic properties of doped barium hexaferrite with BaZn0.6Zr0.3X0.3Fe10.8O19 (X= Ti, Ce, Sn) composition, Iran. J. Phys. Res. 17 (2019) 357–363. https://doi.org/10.18869/acadpub.ijpr.17.3.358.
[119] P. Sharma, R.A. Rocha, S.N. De Medeiros, A. Paesano Jr, Structural and magnetic studies on barium hexaferrites prepared by mechanical alloying and conventional route, J. Alloys Compd. 443 (2007) 37–42. https://doi.org/10.1016/j.jallcom.2006.10.022.
[120] J.L. Snoek, Non Metallic Magnetic Material for High Frequencies, Philips Tech. Rev. 8 (1946) 359.
[121] C. Wu, W. Wang, Q. Li, M. Wei, Q. Luo, et al., Barium hexaferrites with narrow ferrimagnetic resonance linewidth tailored by site-controlled Cu doping, J. Am. Ceram. Soc. 105 (2022) 7492–7501. https://doi.org/10.1111/jace.18702.
[122] X. Wang, H. Yan, S. Zhao, S. Liu, H. Chang, Modifiable natural ferromagnetic resonance frequency and strong microwave absorption in BaFe12-y-2xAlySnxMnxO19 M-type hexaferrite, J. Magn. Magn. Mater. 586 (2023) 171159. https://doi.org/10.1016/j.jmmm.2023.171159.
[123] P.D. Thang, N.H. Tiep, T.A. Ho, N.D. Co, N.T.M. Hong, et al., Electronic structure and multiferroic properties of (Y, Mn)-doped barium hexaferrite compounds, J. Alloys Compd. 867 (2021) 158794. https://doi.org/10.1016/j.jallcom.2021.158794.
[124] S. Verma, A. Singh, S. Sharma, P. Kaur, S.K. Godara, et al., Magnetic and structural analysis of BaZnxZrxFe12–2xO19 (x= 0.1–0.7) hexaferrite samples for magnetic applications, J. Alloys Compd. 930 (2023) 167410. https://doi.org/10.1016/j.jallcom.2022.167410.
[125] S.U. Asif, U.-R. Ghori, Q.A. Ranjha, F. Ahmed, G.F.B. Solre, et al., Impact of ferromagnetic Ni substitution on structural and magnetic parameters of Ba0.8In0.2Fe12−xNixO19 (x= 0.00–2.00) hexaferrites, J. Inorg. Organomet. Polym. Mater. 33 (2023) 2721–2731. https://doi.org/10.1007/s10904-023-02713-w.
[126] A.R. Makhdoom, F. Ahmed, U.-R. Ghori, Q.A. Ranjha, K.A. Rao, et al., Tuning magnetic properties in the Ce–Al Co-substituted M-type BaSr (6: 4) hexaferrites, J. Mater. Sci. Mater. Electron. 33 (2022) 7266–7274. https://doi.org/10.1007/s10854-022-07915-5.
[127] A.A. Ati, A.H. Abdalsalam, A.S. Hasan, Thermal, microstructural and magnetic properties of manganese substitution cobalt ferrite prepared via co-precipitation method, J. Mater. Sci. Mater. Electron. 32 (2021) 3019–3037. https://doi.org/10.1007/s10854-020-05053-4.
[128] K. Habanjar, H. Shehabi, A.M. Abdallah, R. Awad, Effect of calcination temperature and cobalt addition on structural, optical and magnetic properties of barium hexaferrite BaFe12O19 nanoparticles, Appl. Phys. A. 126 (2020) 402. https://doi.org/10.1007/s00339-020-03497-3.
[129] M.M.E. Barakat, D.E.-S. Bakeer, A.-H. Sakr, Structural, magnetic properties and electron paramagnetic resonance for BaFe12-xHgxO19 hexaferrite nanoparticles prepared by co-precipitation method, J. Taibah Univ. Sci. 14 (2020) 640–652. https://doi.org/10.1080/16583655.2020.1761676.
[130] F.J. Santos-López, S. Díaz-Castañón, Magnetic Properties and Electric Hysteresis in SrFe12O19 Hexaferrites at Low Sintered Temperatures, J. Supercond. Nov. Magn. 37 (2024) 881–888. https://doi.org/10.1007/s10948-024-06724-7.
[131] D.D. Parmar, P.N. Dhruv, S.S. Meena, S. Kavita, C.S. Sandhu, et al., Effect of copper substitution on the structural, magnetic, and dielectric properties of M-type lead hexaferrite, J. Electron. Mater. 49 (2020) 6024–6039. https://doi.org/10.1007/s11664-020-08326-0.
[132] R. Kausar, M.A. Khan, S. Gulbadan, M. Junaid, A. Hussain, et al., Investigation into the structural and magnetic features of nickel doped U-type hexaferrites prepared through sol–gel method, J. Magn. Magn. Mater. 549 (2022) 169054. https://doi.org/10.1016/j.jmmm.2022.169054.
[133] M. Jafarian, S.S.S. Afghahi, Y. Atassi, A. Loriamini, Promoting the microwave absorption characteristics in the X band using core-shell structures of Cu metal particles/PPy and hexaferrite/PPy, J. Magn. Magn. Mater. 493 (2020) 165680. https://doi.org/10.1016/j.jmmm.2019.165680.
[134] S.K. Godara, V. Kaur, P.S. Malhi, J. Ahmed, S.M. Alshehri, et al., Sol-gel auto-combustion synthesis of double metal-doped barium hexaferrite nanoparticles for permanent magnet applications, J. Solid State Chem. 312 (2022) 123215. https://doi.org/10.1016/j.jssc.2022.123215.
[135] M.Z. Khan, I.H. Gul, F. Javaid, A. Ali, S. Hafeez, M.M. Baig, Synthesis and characterization of Zr4+-Y3+ substituted Ba-Sr hexaferrite nanoparticles for microwave absorption and electromagnetic shielding applications, Mater. Res. Bull. 168 (2023) 112468. https://doi.org/10.1016/j.materresbull.2023.112468.
[136] V.P. Singh, R. Jasrotia, R. Kumar, P. Raizada, S. Thakur, et al., A current review on the synthesis and magnetic properties of M-type hexaferrites material, World J. Condens. Matter. Phys. 8 (2018) 36. https://doi.org/10.4236/wjcmp.2018.82004.
[137] Z. Mosleh, P. Kameli, A. Poorbaferani, M. Ranjbar, H. Salamati, Structural, magnetic and microwave absorption properties of Ce-doped barium hexaferrite, J. Magn. Magn. Mater. 397 (2016) 101–107. https://doi.org/10.1016/j.jmmm.2015.08.078.
[138] S.K. Godara, M.P. Kaur, V. Kaur, P.S. Malhi, M. Singh, et al., Investigation of microstructural and magnetic properties of Ca2+ doped strontium hexaferrite nanoparticles, J. King Saud Univ. 34 (2022) 101963. https://doi.org/10.1016/j.jksus.2022.101963.
[139] G.B. Todkar, R.A. Kunale, R.N. Kamble, K.M. Batoo, M.F. Ijaz, et al., Ce–Dy substituted barium hexaferrite nanoparticles with large coercivity for permanent magnet and microwave absorber application, J. Phys. D. Appl. Phys. 54 (2021) 294001. https://doi.org/10.1088/1361-6463/abf864.
[140] A. Karimian, M. Kalantar, Magnetic, gas sensing properties, and structural parameters of barium–calcium hexaferrite synthesized

by sol-gel auto combustion method, J. Chin. Chem. Soc. 69 (2022) 450−461. https://doi.org/10.1002/jccs.202100417.
[141] M.K. Manglam, S. Kumari, J. Mallick, M. Kar, Crystal structure and magnetic properties study on barium hexaferrite of different average crystallite size, Appl. Phys. A. 127 (2021) 1–12. https://doi.org/10.1007/s00339-020-04232-8.
[142] S.K. Godara, J. Prakash, R. Jasrotia, J. Ahmed, A.M. Tamboli, et al., Green synthesis of magnetic nanoparticles of BaFe12O19 hexaferrites using tomato pulp: structural, morphological, optical, magnetic and dielectric traits, J. Mater. Sci. Mater. Electron. 34 (2023) 1516. https://doi.org/10.1007/s10854-023-10859-z.
[143] W. Liao, K. Huang, W. Xu, J. Yu, P. Li, J. Xu, Broadband microwave absorption and electromagnetic properties of Gd–Al–Co-doped M− type barium hexaferrite in 2–18 GHz range, J. Magn. Magn. Mater. (2024) 172609. https://doi.org/10.1016/j.jmmm.2024.172609.
[144] A.Y. Mironovich, V.G. Kostishin, R.I. Shakirzyanov, A.A. Mukabenov, S.A. Melnikov, et al., Effect of the Fe/Ba and Fe/Sr ratios on the phase composition, dielectric properties and magnetic characteristics of M-type hexaferrites prepared by the hydrothermal method, J. Solid State Chem. 316 (2022) 123625. https://doi.org/10.1016/j.jssc.2022.123625.
[145] L. Peibo, S. Yize, Y. Akinay, The influence of MWCNTs on microwave absorption properties of Co/C and Ba-Hexaferrite hybrid nanocomposites, Synth. Met. 263 (2020) 116369. https://doi.org/10.1016/j.synthmet.2020.116369.
[146] Y. Jing, L. Jia, Y. Zheng, H. Zhang, Hydrothermal synthesis and competitive growth of flake-like M-type strontium hexaferrite, RSC Adv. 9 (2019) 33388–33394. https://doi.org/10.1039/C9RA06246G.
[147] I. Mohammed, J. Mohammed, A.U. Kende, A.M. Wara, Y.A. Aliero, et al., Review on Y-type hexaferrite: Synthesis, characterization and properties, Appl. Surf. Sci. Adv. 16 (2023) 100416. https://doi.org/10.1016/j.apsadv.2023.100416.
[148] A.Y. Mironovich, V.G. Kostishin, H.I. Al-Khafaji, A.V. Timofeev, A.I. Ril, et al., Magnetic and structural properties of Co-substituted barium hexaferrite synthesized by hydrothermal method, J. Magn. Magn. Mater. 588 (2023) 171469. https://doi.org/10.1016/j.jmmm.2023.171469.
[149] K.T. Selvi, M. Priya, Effect of Co and Sm substitutions on the magnetic interactions of M-type strontium hexaferrite nanoparticles, J. Supercond. Nov. Magn. 33 (2020) 713–720. https://doi.org/10.1007/s10948-019-05227-0.
[150] S.L. Hu, J. Liu, H.Y. Yu, Z.W. Liu, Synthesis and properties of barium ferrite nano-powders by chemical co-precipitation method, J. Magn. Magn. Mater. 473 (2019) 79–84. https://doi.org/10.1016/j.jmmm.2018.10.044.
[151] S.U. Asif, G.F.B. Solre, E.A.M. Saleh, A.M. Saeedi, M.M. Moharam, et al., Structural and Magnetic Impressions of Rare Earth Tb Doping on Ba–In Based Hexaferrites Prepared Through Sol–Gel Route for Magnetic Aspects, J. Inorg. Organomet. Polym. Mater. 34 (2024) 1–12. https://doi.org/10.1007/s10904-023-02989-y.
[152] W.M. Shoubak, A. Hassan, S. Mahrous, A. Hassen, Controlling the physical properties of polyacrylonitrile by strontium hexaferrite nanoparticles, Polym. Bull. 81 (2024) 697–718. https://doi.org/10.1007/s00289-023-04736-2.
[153] R. Islam, K. Vero, J.P. Borah, Historical overview and recent advances in permanent magnet materials, Mater. Today Commun. 41 (2024) 110538. https://doi.org/10.1016/j.mtcomm.2024.110538.
[154] S. Wang, H. Gao, G. Sun, J. Zhang, Y. Xia, et al., M-type barium hexaferrite nanoparticles synthesized by γ-ray irradiation assisted polyacrylamide gel method and its optical, magnetic and supercapacitive performances, J. Clust. Sci. 32 (2021) 569–578. https://doi.org/10.1007/s10876-020-01815-6.
[155] S.B. Narang, K. Pubby, Nickel spinel ferrites: a review, J. Magn. Magn. Mater. 519 (2021) 167163. https://doi.org/10.1016/j.jmmm.2020.167163.
[156] P. Li, J. Li, Y. Wang, K. Yao, S. Shan, et al., Structural, spectral, and magnetic properties of praseodymium–aluminum-co-doped M-type barium hexaferrites, J. Supercond. Nov. Magn. 36 (2023) 327–341. https://doi.org/10.1007/s10948-022-06445-9.
[157] F.F. Alharbi, S. Aman, N. Ahmad, S.R. Ejaz, R.Y. Khosa, et al., Eu–Co substituted Sr-hexaferrites for recording media and microwave devices, J. Mater. Sci. Mater. Electron. 33 (2022) 12147–12156. https://doi.org/10.1007/s10854-022-08175-z.
[158] K. Için, S. Öztürk, D.D. Çakıl, S.E. Sünbül, İ. Ergin, B. Özçelik, Investigation of nano-crystaline strontium hexaferrite magnet powder from mill scale waste by the mechanochemical synthesis: Effect of the annealing temperature, Mater. Chem. Phys. 290 (2022) 126513. https://doi.org/10.1016/j.matchemphys.2022.126513.
[159] A.R. Al Dairy, L.A. Al-Hmoud, H.A. Khatatbeh, Magnetic and structural properties of barium hexaferrite nanoparticles doped with titanium, Symmetry (Basel). 11 (2019) 732. https://doi.org/10.3390/sym11060732.
[160] A. Dong, R. Liu, Z. Tian, F. Peng, R. Zhao, et al., Effect of pre-sintering particle size on the microstructure and magnetic properties of two-step hot-press prepared BaFe12O19 thick films, J. Alloys Compd. 967 (2023) 171683. https://doi.org/10.1016/j.jallcom.2023.171683.
[161] Y. Zou, J. Lin, W. Zhou, M. Yu, J. Deng, et al., Coexistence of high magnetic and dielectric properties in Ni-Zr co-doped barium hexaferrites, J. Alloys Compd. 907 (2022) 164516. https://doi.org/10.1016/j.jallcom.2022.164516.
[162] A. Kumar, R.K. Singh, H.K. Satyapal, A. Kumar, S. Sharma, Lattice strain mediated structural and magnetic properties enhancement of strontium hexaferrite nanomaterials through controlled annealing, Phys. B: Condens. Matter. 600 (2021) 412592. https://doi.org/10.1016/j.physb.2020.412592.
[163] M.A. Almessiere, Y. Slimani, N.A. Tashkandi, A. Baykal, M.F. Saraç, et al., The effect of Nb substitution on magnetic properties of BaFe12O19 nanohexaferrites, Ceram. Int. 45 (2019) 1691–1697. https://doi.org/10.1016/j.ceramint.2018.10.048.
[164] J. Han, H. Wang, Investigation effect of Lu-substitution on structural, morphological, magnetic, and dielectric properties of BaM hexaferrite synthesized using a co-precipitation method, Mater. Today Commun. 38 (2024) 108148. https://doi.org/10.1016/j.mtcomm.2024.108148.
[165] W. Tahir, M.A. Khan, R.T. Rasool, S. Gulbadan, A. Majeed, G. Nasar, Structural, Raman, Photo luminance, morphological, and magnetic properties of Sr-Ba-Cu–Zn W-type hexaferrites, J. Mater. Sci. Mater. Electron. 34 (2023) 1812. https://doi.org/10.1007/s10854-023-11192-1.
[166] S. Chanda, S. Bharadwaj, A. Srinivas, K.V.S. Kumar, Y.K. Lakshmi, Estimation of iron ion distribution at various sites contributing to saturation magnetization in barium hexaferrite at different sintering temperatures, J. Phys. Chem. Solids. 155 (2021) 110120. https://doi.org/10.1016/j.jpcs.2021.110120.
[167] N. Parween, Study of barium hexaferrite (BaFe12O19) synthesised by sol gel auto-combustion technique, Master of Science Thesis, National Institute of Technology, Rourkela, India. (2014).
[168] S. Prathap, W. Madhuri, S.S. Meena, Effect of non-stoichiometry in lead hexaferrites on magnetic and dielectric properties, Mater. Chem. Phys. 220 (2018) 137–148. https://doi.org/10.1016/j.matchemphys.2018.08.034.
[169] Y. Dai, Z. Lan, Z. Yu, K. Sun, R. Guo, et al., Effects of La substitution on micromorphology, static magnetic properties and low ferromagnetic resonance linewidth of self-biased M-type Sr hexaferrites for high frequency application, Ceram. Int. 47 (2021) 8980–8986. https://doi.org/10.1016/j.ceramint.2020.12.020.
[170] E.A. Gorbachev, L.A. Trusov, L.N. Alyabyeva, I.V Roslyakov, V.A. Lebedev, et al., High-coercivity hexaferrite ceramics featuring sub-terahertz ferromagnetic resonance, Mater. Horizons. 9 (2022) 1264–1272. https://doi.org/10.1039/D1MH01797G.

[171] S. Lu, Y. Liu, Q. Yin, J. Chen, J. Li, J. Wu, Effects of Ce-Zn co-substitution on the structural and magnetic properties of M-type barium hexaferrites, J. Magn. Magn. Mater. 564 (2022) 170068. https://doi.org/10.1016/j.jmmm.2022.170068.

[172] Y. He, R. Wang, X. Wu, C. Tang, J. Qian, et al., The combined sol-gel and ascorbic acid reduction strategy enabling Ba2Co2Fe12O22 hexaferrite/graphene composite with enhanced microwave absorption ability, Mater. Res. Bull. 174 (2024) 112721. https://doi.org/10.1016/j.materresbull.2024.112721.

[173] S.S. Veisi, M. Yousefi, M.M. Amini, A.R. Shakeri, M. Bagherzadeh, S.S.S. Afghahi, Magnetic properties, structural studies and microwave absorption performance of Ba0.5Sr0.5CuxZrxFe12-2xO19/Poly Ortho-Toluidine (X= 0.2, 0.4, 0.6, 0.8) ceramic nanocomposites, Inorg. Chem. Commun. 132 (2021) 108802. https://doi.org/10.1016/j.inoche.2021.108802.

[174] F. Xu, L. Ma, M. Gan, J. Tang, Z. Li, et al., Preparation and characterization of chiral polyaniline/barium hexaferrite composite with enhanced microwave absorbing properties, J. Alloys Compd. 593 (2014) 24–29. https://doi.org/10.1016/j.jallcom.2014.01.032.

[175] P. Bhattacharya, S. Dhibar, G. Hatui, A. Mandal, T. Das, C. K. Das, Graphene decorated with hexagonal shaped M-type ferrite and polyaniline wrapper: a potential candidate for electromagnetic wave absorbing and energy storage device applications, RSC Adv. 4 (2014) 17039–17053. https://doi.org/10.1039/C4RA00448E.

[176] K.S. Sista, S. Dwarapudi, D. Kumar, G.R. Sinha, A.P. Moon, Carbonyl iron powders as absorption material for microwave interference shielding: A review, J. Alloys Compd. 853 (2021) 157251. https://doi.org/10.1016/j.jallcom.2020.157251.

[177] C. Zhang, Z. Wu, C. Xu, B. Yang, L. Wang, et al., Hierarchical Ti3C2Tx MXene/carbon nanotubes hollow microsphere with confined magnetic nanospheres for broadband microwave absorption, Small. 18 (2022) 2104380. https://doi.org/10.1002/smll.202104380.

[178] S. Goel, M. Bala, A. Garg, V.D. Shivling, S. Tyagi, Lanthanum doped barium hexaferrite nanoparticles for enhanced microwave absorption, Mater. Today Proc. 28 (2020) 1753–1758. https://doi.org/10.1016/j.matpr.2020.05.157.

[179] I.M. Yar, M. Irfan, F. Naheed, M.N. Akhtar, R.T. Rasool, et al., Dielectric, physicochemical, and reflection loss features of Gd-substituted W-type hexaferrites for microwave absorption application, Appl. Phys. A. 130 (2024) 87. https://doi.org/10.1007/s00339-023-07227-3.

[180] M. Chang, Q. Li, Z. Jia, W. Zhao, G. Wu, Tuning microwave absorption properties of Ti3C2Tx MXene-based materials: Component optimization and structure modulation, J. Mater. Sci. Technol. 148 (2023) 150–170. https://doi.org/10.1016/j.jmst.2022.11.021.

[181] X. Zhao, Y. Huang, X. Liu, J. Yan, L. Ding, et al., Core-shell CoFe2O4@C nanoparticles coupled with rGO for strong wideband microwave absorption, J. Colloid Interface Sci. 607 (2022) 192–202. https://doi.org/10.1016/j.jcis.2021.08.203.

[182] S.A. Mathews, D.R. Babu, Analysis of the role of M-type hexaferrite-based materials in electromagnetic interference shielding, Curr. Appl. Phys. 29 (2021) 39–53. https://doi.org/10.1016/j.cap.2021.06.001.

[183] D. Xu, M. Jafarian, S.S.S. Afghahi, Y. Atassi, R.A.-Q.B. Al-Marjeh, Remarkable microwave absorption efficiency of low loading ratio of Ni0.25Co0.25Ti0.5Fe2O4/SrCoTiFe10O19/Cu composite coated with polyprrole within polyurethane matrix, Mater. Res. Express. 7 (2020) 16103. https://doi.org/10.1088/2053-1591/ab62f1.

[184] H. Yan, Y. Guo, X. Bai, J. Qi, H. Lu, Facile constructing Ti3C2Tx/TiO2@C heterostructures for excellent microwave absorption properties, J. Colloid Interface Sci. 654 (2024) 1483–1491. https://doi.org/10.1016/j.jcis.2023.10.076.

[185] F. Chen, S. Zhang, B. Ma, Y. Xiong, H. Luo, et al., Bimetallic CoFe-MOF@Ti3C2Tx MXene derived composites for broadband microwave absorption, Chem. Eng. J. 431 (2022) 134007. https://doi.org/10.1016/j.cej.2021.134007.

[186] M.A. Almessiere, Y. Slimani, A.V. Trukhanov, A. Sadaqat, A.D. Korkmaz, et al., Review on functional bi-component nanocomposites based on hard/soft ferrites: structural, magnetic, electrical and microwave absorption properties, Nano-Struct. Nano-Objects. 26 (2021) 100728. https://doi.org/10.1016/j.nanoso.2021.100728.

[187] E.E. Ateia, K. Elsayed, D.E. El-Nashar, Tuning the properties of NBR/BaFe11.5Co0.5O19: a road toward diverse applications, Appl. Phys. A. 129 (2023) 118. https://doi.org/10.1007/s00339-023-06388-5.

[188] W. Xu, W. Liao, H. Zhou, L. Wang, K. Huang, et al., M-Type Ba-Hexaferrite Nanoplates with Exceptional Microwave Absorption Properties, ACS Appl. Electron. Mater. 6 (2024) 2759–2766. https://doi.org/10.1021/acsaelm.4c00307.

[189] S.S.S. Afghahi, M. Jafarian, Y. Atassi, Microstructural and magnetic studies on BaMgxZnxX2xFe12−4xO19 (X= Zr, Ce, Sn) prepared via mechanical activation method to act as a microwave absorber in X-band, J. Magn. Magn. Mater. 406 (2016) 184–191. https://doi.org/10.1016/j.jmmm.2016.01.020.

[190] H. Li, L. Zheng, D. Deng, X. Yi, X. Zhang, et al., Multiple natural resonances broaden microwave absorption bandwidth of substituted M-type hexaferrites, J. Alloys Compd. 862 (2021) 158638. https://doi.org/10.1016/j.jallcom.2021.158638.

[191] A. Garg, S. Goel, A.K. Dixit, M.K. Pandey, N. Kumari, S. Tyagi, Investigation on the effect of neodymium doping on the magnetic, dielectric and microwave absorption properties of strontium hexaferrite particles in X-band, Mater. Chem. Phys. 257 (2021) 123771. https://doi.org/10.1016/j.matchemphys.2020.123771.

[192] A. Garg, S. Goel, N. Kumari, P. Soni, H.B. Baskey, S. Tyagi, Yttrium-doped strontium hexaferrite particles for microwave absorption application in X-band, J. Mater. Sci. Mater. Electron. 31 (2020) 13746–13755. https://doi.org/10.1007/s10854-020-03934-2.

[193] H.H. Nguyen, N. Tran, T.L. Phan, D.S. Yang, N.T. Dang, B.W. Lee, Electronic structure, and magnetic and microwave absorption properties of Co-doped SrFe12O19 hexaferrites, Ceram. Int. 46 (2020) 19506–19513. https://doi.org/10.1016/j.ceramint.2020.04.304.

[194] V.K. Chakradhary, M.J. Akhtar, Highly coercive strontium hexaferrite nanodisks for microwave absorption and other industrial applications, Compos. B: Eng. 183 (2020) 107667. https://doi.org/10.1016/j.compositesb.2019.107667.

[195] M. Rostami, M. Jafarpour, M.H.M. Ara, An investigation on the microwave absorption properties of Co–Al–Ti substituted barium hexaferrite-MWCNT nanocomposites, J. Alloys Compd. 872 (2021) 159656. https://doi.org/10.1016/j.jallcom.2021.159656.

[196] S. Goel, A. Garg, H.B. Baskey, S. Tyagi, Microwave absorption study of low-density composites of barium hexaferrite and carbon black in X-band, J. Sol-Gel Sci. Technol. 98 (2021) 351–363. https://doi.org/10.1007/s10971-021-05492-3.

[197] X. Liu, R. Ji, M. Yang, W. Chen, H. Chen, et al., Facilitating enhanced microwave absorption properties of barium hexaferrite/polyaniline composites based on tunable interfacial polarization by rare earth doping, J. Alloys Compd. 937 (2023) 168391. https://doi.org/10.1016/j.jallcom.2022.168391.

[198] V. Sharma, S. Kumari, B.K. Kuanr, Rare earth doped M-type hexaferrites; ferromagnetic resonance and magnetization dynamics, Aip Adv. 8 (2018) 056232. https://doi.org/10.1063/1.5007297.

[199] F. Ebrahimi, F. Ashrafizadeh, Tuning the ferromagnetic resonance by doping strontium hexa-ferrite nanopowders, J. Sol-Gel Sci. Technol. 85 (2018) 621–628. https://doi.org/10.1007/s10971-018-4578-1.